Research Paper

GEOSPHERE

GEOSPHERE

https://doi.org/10.1130/GES02580.1

18 figures; 2 tables; 1 set of supplemental files

CORRESPONDENCE: Andrea.Balbas@csulb.edu

CITATION: Sotomayor, A., Balbas, A., Konrad, K., Koppers, A.A.P., Konter, J.G., Dorset Wanless, V., Hourigan, T.F., Kelley, C., and Raineault, N., 2023, New insights into the age and origin of two small Cretaceous seamount chains proximal to the Northwestern Hawaiian Ridge: Geosphere, https://doi.org/10.1130/GES02580.1.

Science Editor: Christopher J. Spencer

Received 30 July 2022
Revision received 24 October 2022
Accepted 24 December 2022

Published online 2 March 2023

New insights into the age and origin of two small Cretaceous seamount chains proximal to the Northwestern Hawaiian Ridge

Arturo Sotomayor[1], Andrea Balbas[1], Kevin Konrad[2], Anthony A.P. Koppers[3], Jasper G. Konter[4], V. Dorsey Wanless[5], Thomas F. Hourigan[6], Christopher Kelley[4], and Nicole Raineault[7]

[1]Department of Geological Sciences, California State University Long Beach, Long Beach, California 90840, USA
[2]Department of Geoscience, University of Nevada, Las Vegas, Las Vegas, Nevada 89154, USA
[3]College of Earth, Ocean, and Atmospheric Sciences, Oregon State University, Corvallis, Oregon 97331, USA
[4]Department of Earth Sciences, University of Hawaii–Manoa, Honolulu, Hawaii 96822, USA
[5]Department of Geosciences, Boise State University, Boise, Idaho 83725, USA
[6]National Oceanic and Atmospheric Administration, National Marine Fisheries Service, Deep Sea Coral Research and Technology Program, Silver Spring, Maryland 20910, USA
[7]Florida Institute of Oceanography, St. Petersburg, Florida 33701, USA

ABSTRACT

The Northwestern Hawaiian Ridge is an age-progressive volcanic chain sourced from the Hawaiian mantle plume. Proximal to the Northwestern Hawaiian Ridge are several clusters of smaller seamounts and ridges with limited age constraints and unknown geodynamic origins. This study presents new bathymetric data and $^{40}Ar/^{39}Ar$ age determinations from lava flow samples recovered by remotely operated vehicle (ROV) from two east–west-trending chains of seamounts that lie north of the Pūhāhonu and Mokumanamana volcanoes. The previously unexplored Naifeh Chain (28°48′N,167°48′W) and Plumeria Chain (25°36′N, 164°35′W) contain five volcanic structures each, including three guyots in the Naifeh Chain. New $^{40}Ar/^{39}Ar$ age determinations indicate that the Naifeh Chain formed ca. 88 Ma and the Plumeria Chain ca. 85 Ma. The Cretaceous ages, coupled with a perpendicular orientation of the seamounts relative to absolute Pacific plate motion at that time, eliminate either a Miocene Hawaiian volcanic arch or Cretaceous mantle-plume origin. The seamounts lie on oceanic crust that is modeled to be 10–15 Ma older than the corresponding seamounts. Here, two models are put forth to explain the origin of these enigmatic seamount chains as well as the similar nearby Mendelssohn Seamounts. (1) Diffuse lithospheric extension results in the formation of these seamounts until the initiation of the Kula-Pacific spreading center in the north at 84–79 Ma, which alleviates the tension. (2) Shear-driven upwelling of enriched mantle material beneath young oceanic lithosphere results in an age-progressive seamount track that is approximately perpendicular to the spreading ridge. Here we show that all sampled seamounts proximal to the Northwestern Hawaiian Ridge are intraplate in nature, but their formations can be attributed to both plume and plate processes.

INTRODUCTION

Understanding the geodynamic origin and mantle sources of intraplate volcanism is vital to discerning the drivers of volcanism, the composition of Earth's interior, and past plate motions. Most large (>3 km in height) intraplate seamounts and islands are hypothesized to be sourced from mantle-plume processes (Morgan, 1972; Wessel et al., 2010; Koppers et al., 2021). These thermochemical upwellings of deep mantle material produce age-progressive seamount chains that can persist for over 100 Ma as a plate moves over the approximately stationary hotspot. However, numerous seamounts and volcanic ridges within the ocean basins lack clear age-progressions or geographic trends that match paleo-plate motion (e.g., Sandwell et al., 1995; Davis et al., 2002; Castillo et al., 2010). A diverse range of processes that produce non-age–progressive volcanism or age-progressive volcanism that is inconsistent with absolute plate motion have been proposed, including independent plume motion (e.g., Steinberger, 2000; Steinberger et al., 2004; Konrad et al., 2018), edge-driven convection (King and Anderson, 1998), asthenospheric shear-driven upwelling (Conrad et al., 2011; Ballmer et al., 2013), lithospheric detachment (Hoernle et al., 2006), plate-flexure processes (Hirano et al., 2006; Konter and Jackson, 2012), and extensional processes (Sandwell et al., 1995; Janney et al., 2000; Davis et al., 2002).

Extension-derived oceanic intraplate volcanism has been described for regions experiencing changing plate boundaries (Davis et al., 2010) and tension above unusually enriched shallow mantle (Janney et al., 2000), and during times of plate motion shifts, such as the ca. 50 Ma global plate reorganization event (O'Connor et al., 2015). However, some studies have indicated that lithospheric extension can reduce or prevent melting rather than induce volcanism (e.g., McKenzie and Bickle, 1988). For seamounts formed on young oceanic crust, high rates of asthenospheric shear—the shear generated from large-scale mantle flow moving in an opposite direction from lithospheric spreading/plate motion—are found within regions with the highest densities of low-volume, non-plume–related volcanism in the Pacific Basin (Conrad et al., 2011). These

Andrea Balbas https://orcid.org/0000-0002-4855-3507

shear zones interact with viscosity heterogeneities to generate localized, shear-driven upwelling (SDU) that can produce intraplate volcanism (Conrad et al., 2010). There are multiple ways to produce intraplate volcanism in the ocean basins, and detailed sampling is required to better constrain these processes throughout deep time.

To date, most seamount sampling expeditions have focused on large seamount chains to test hypotheses regarding plate motion and mantle-plume dynamics. However, the ocean basins are covered in small seamount clusters and chains that often go unexplored. The formation mechanisms for these small seamount clusters are often not associated with mantle-plume processes and thus have the potential to provide important constraints on past plate dynamics. Here, we present new high-resolution multibeam data and age-determination results for previously unexplored seamounts that lie just north of Pūhāhonu (Gardner Pinnacles) and Mokumanamana (Necker Island), Pacific Ocean (Figs. 1 and 2). The age and geography of these seamounts eliminate both an on-ridge and mantle-plume origin, and thus they provide new information on potential plate drivers for intraplate volcanism.

GEOLOGIC SETTING

The Northwestern Hawaiian Ridge is a linear series of islands, atolls, and seamounts that extend from the Hawaiian Islands to the Hawaiian-Emperor Bend (Fig. 1). Surrounding the Northwestern Hawaiian Ridge are numerous, typically Cretaceous-aged seamounts that are less well understood and have been suggested to be related to ancient mantle plumes or on/near-ridge processes. These ancient features include the Hess Rise (ca. 100 Ma), Liliuokalani Ridge (southernmost seamount is 75 Ma), Geologist Seamounts (ca. 86–78 Ma), and the Musician Seamounts and Ridges (98–76 Ma and 53–49 Ma; Garcia et al., 1987; Pringle, 1992; Pringle and Dalrymple, 1993; O'Connor et al., 2015; Fig. 2). This study focuses on two chains of E–W-trending seamounts that lie just north of Pūhāhonu (Gardner Pinnacle) and Mokumanamana (Necker Seamount), Northwestern Hawaiian Ridge (Fig. 2). The previously unexplored Naifeh and Plumeria chains were mapped with ship-based multibeam sonar and sampled via the Ocean Exploration Trust's remotely operated vehicle (ROV) *Hercules* during the NA101 expedition of the E/V *Nautilus* (September–October 2018; Kelley et al., 2019).

New multibeam data indicate that the two chains include five seamounts and/or guyots each (Fig. 3). The Naifeh Chain is named after Naifeh Guyot. This chain includes three large guyot structures and two smaller conical seamounts that are aligned in a general E–W trend (~100° heading azimuth; Fig. 3A). The second chain of five mapped seamounts has no official name, so we refer to it here as the Plumeria Chain. Its seamounts are smaller and tend to display individual elongated E–W ridge-like morphology that is aligned approximately perpendicular to the regional abyssal hill fabric (Fig. 3B). Preliminary X-ray fluorescence spectrometry (XRF) data from seamount lava flows indicate that the lava are alkaline in composition and primarily trachybasalt to basaltic trachyandesites (Montour et al., 2021; Pasqualon et al., 2022; Fig. 4). To constrain the origin of the Naifeh and Plumeria chains, geomorphological analysis and $^{40}Ar/^{39}Ar$ geochronology were employed to define the time of emplacement of these seamounts and their relationship to surrounding volcanic structures within the Pacific Basin. Each newly explored seamount is described in detail in the Results section below.

Immediately to the east of the Plumeria Chain lies the small, E–W-trending Mendelssohn Ridge, which is comprised of two seamounts (Sager and Pringle, 1987; Fig. 5). These seamounts were dredged in 1980 and displayed $^{40}Ar/^{39}Ar$ incremental heating ages of 84.2 ± 1.3 Ma (2σ; Mendelssohn West) and 80.2 ± 0.9 Ma (Mendelssohn East) (Sager and Pringle, 1987). The Mendelssohn Seamounts were argued to be the southernmost extent of the age-progressive Musician Chain (Fig. 2; Sager and Pringle, 1987); however, their relationship to the proposed Euterpe Plume has been questioned (Kopp et al., 2003). The two Mendelssohn seamounts are 4–8 Ma younger than Haydn Seamount and Bach Ridge, which lie 160 km to the north, complicating linear age progressions (Kopp et al., 2003). Therefore, we incorporate the Mendelssohn Seamounts as part of a larger E–W seamount trend along with the Naifeh and Plumeria chains in our discussion below.

METHODS

Bathymetric Data Processing and Analyses

Multibeam bathymetric data was collected during the 2018 E/V *Nautilus* expedition NA101 using a Kongsberg EM 302 multibeam echo sounder. Bathymetric data was processed and analyzed using the QPS geomatics software suite. Qimera was used for multibeam editing, and a spline filter was employed to smooth noisy echo sounder data followed by manual slice editing to remove remaining erroneous data. Fledermaus and Esri ArcGIS was used to explore, analyze, and display the processed bathymetric results. Surface area and total volume were calculated by highlighting the swaths that outline the seamounts and running a surface statistical analysis. Slope angles were acquired by running the profile tool along the desired transect and averaging the values. Multibeam data for regions surrounding the two chains studied were obtained from the National Oceanic and Atmospheric Administration (NOAA) digital archives and the General Bathymetric Charts of the Ocean (GEBCO) digital archives (Weatherall et al., 2015).

$^{40}Ar/^{39}Ar$ Age-Determination Methodology

During the NA101 expedition, 53 bulk rock samples from the Naifeh and Plumeria chains were collected from eight of the 10 seamounts using *Hercules*. Links to ROV footage of sampling sites are available in the Supplemental Material[1]. Rock samples from the Naifeh and Plumeria chains that

[1]Supplemental Material. Includes raw data for $^{40}Ar/^{39}Ar$ age determinations and metadata related to sample collection. Please visit https://doi.org/10.1130/GEOS.S.21957038 to access the supplemental material, and contact editing@geosociety.org with any questions.

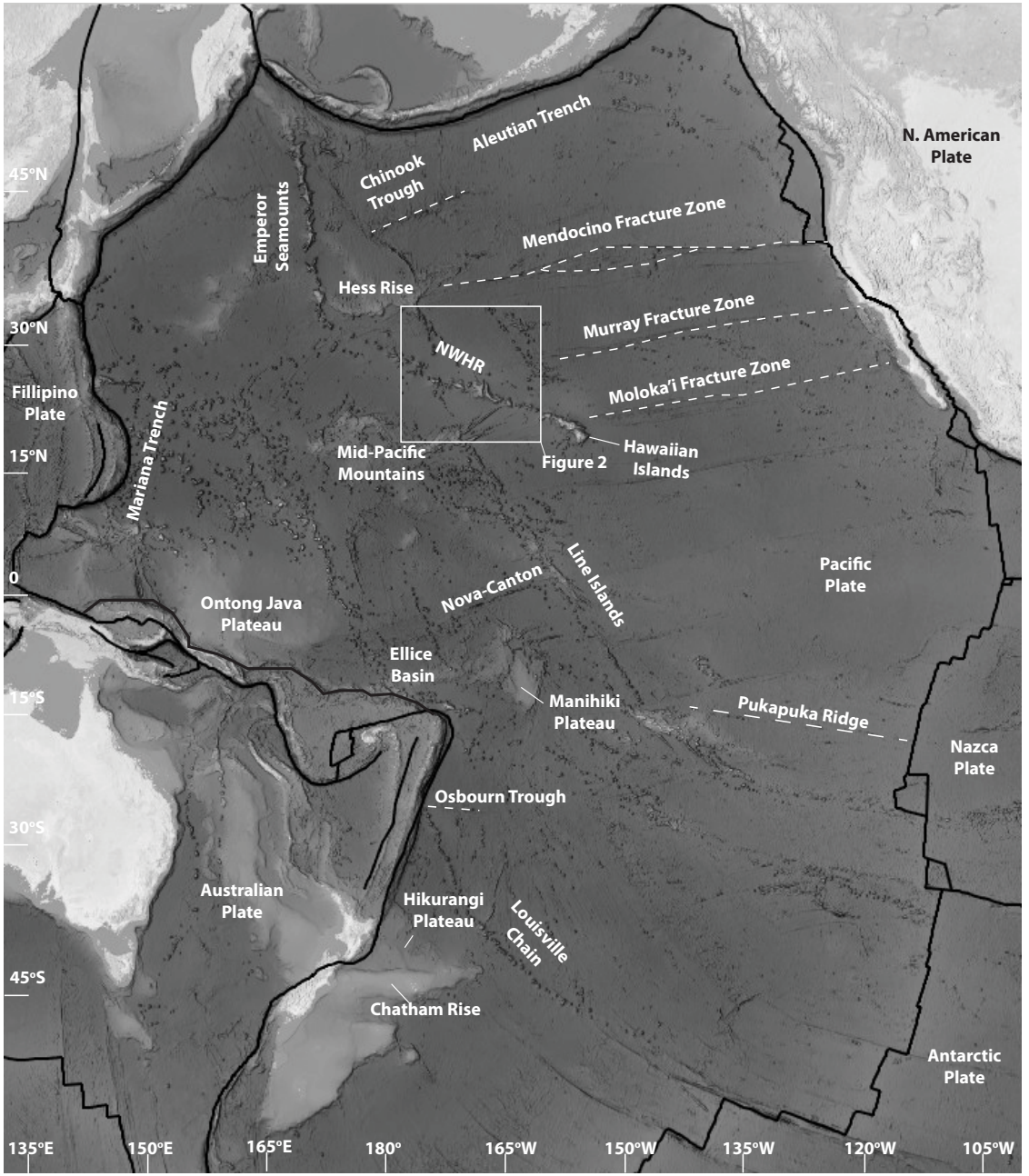

Figure 1. Overview map shows the Pacific Basin. Key structures that pertain to the study such as plateaus, fracture zones, troughs, and chains are outlined along the Pacific plate. A white box near the Hawaiian Islands highlights the study area within the general Northwestern Hawaiian Ridge (NWHR) region.

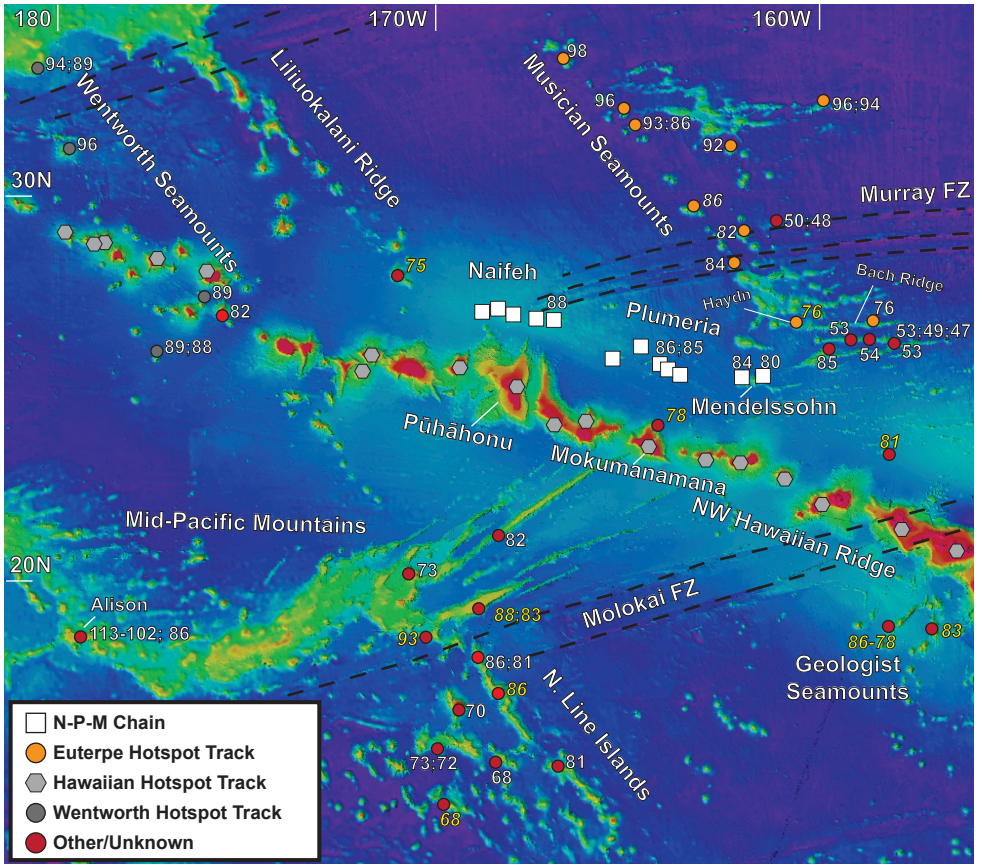

Figure 2. A bathymetric map of the study region is shown, with major features labeled (GEBCO database; Weatherall et al., 2015). Age-dated features are shown with circles (hotspot tracks/unknown origins) or squares for the Naifeh–Plumeria–Mendelssohn (N-P-M) chains. Ages are in Ma and represent either $^{40}Ar/^{39}Ar$ incremental heating experiments or total fusion/K-Ar ages (italic text). Total fusion and K-Ar ages for ancient submarine lava flows should be interpreted with caution (Kelley, 2002). Fracture zones (FZ) are highlighted with black dashed lines.

were chosen for age determinations were all alkaline and composed of a mixture of plagioclase rich-basalts with some olivine and/or clinopyroxene phyric basalts. Plagioclase and groundmass separates were prepared from 15 basalt samples, which cover eight seamounts, following the methods outlined in Konrad et al. (2018) and Balbas et al. (2016).

Separates were produced by sequential crushing, rinsing, sieving, and magnetic separation followed by acid leaching in a heated, sonicated bath (3N HCl; 6N HCl; 1N HNO_3; 3N HNO_3 + 15 min in 5% HF for plagioclase). Samples were irradiated for six hours at the Oregon State University (OSU) TRIGA reactor alongside Fish Canyon Tuff sanidine fluence monitors. Separates were incrementally heated using a CO_2 laser and gases were purified by a series of getters in a stainless-steel extraction line. Incremental heating for marine rocks utilized a detailed 20–30 or 30–40 heating step approach for plagioclase and groundmass separates, respectively.

Argon isotopes were analyzed using an ARGUS VI mass spectrometer housed at OSU. All age determinations were calculated using ArArCalc v.2.7.0 (Koppers, 2002) assuming a Fish Canyon Tuff sanidine age of 28.201 ± 0.046 Ma (2σ; Kuiper et al., 2008) and a total decay constant of 5.530 ± 0.097 × 10^{-10} a^{-1} (2σ; Min et al., 2000). Uncertainties are presented at the 2σ level and include propagated errors associated with blank corrections, collector calibrations, mass discrimination factors, analytical regressions, J-curve calculations, and post-irradiation decay of ^{37}Ar and ^{39}Ar. External uncertainties that include the decay constant and fluence monitor age for each of the 15 samples are included with the full experiment data summary files in the Supplemental Material (see footnote 1).

RESULTS

$^{40}Ar/^{39}Ar$ Geochronology

The new $^{40}Ar/^{39}Ar$ age determinations from the Naifeh and Plumeria chains indicate a formation age of ca. 88 Ma and 85 Ma, respectively (Fig. 6; Table 1). Fifteen $^{40}Ar/^{39}Ar$ experiments were undertaken on 13 different basalt samples covering eight seamounts with only three experiments providing robust data. Two plagioclase mineral separates from Seamount 3 of the Plumeria Chain, NA101-074 and NA101-078, produced concordant mini-plateau (e.g., 40–50% ^{39}Ar) and plateau ages (>50% ^{39}Ar) of 85.63 ± 0.23 Ma (P = 0.09; $^{40}Ar/^{36}Ar_{int}$ = 289 ± 23; ^{39}Ar = 44%) and 84.70 ± 0.22 Ma (P = 0.05; $^{40}Ar/^{36}Ar_{int}$ = 284 ± 19; ^{39}Ar = 59%; Fig. 6). From the Naifeh Chain, a groundmass separate from NA101-007 (Seamount 6) produced a concordant mini-plateau age of 87.72 ± 0.20 Ma (P = 0.30; $^{40}Ar/^{36}Ar_{int}$ = 258 ± 59; Fig. 6), consisting of 42% of ^{39}Ar released, followed by an extended high temperature/excess Ar recoil pattern. The remaining plagioclase separates (n = 7) were marred by multiple excess Ar domains, coupled with low-degree sericitization that resulted

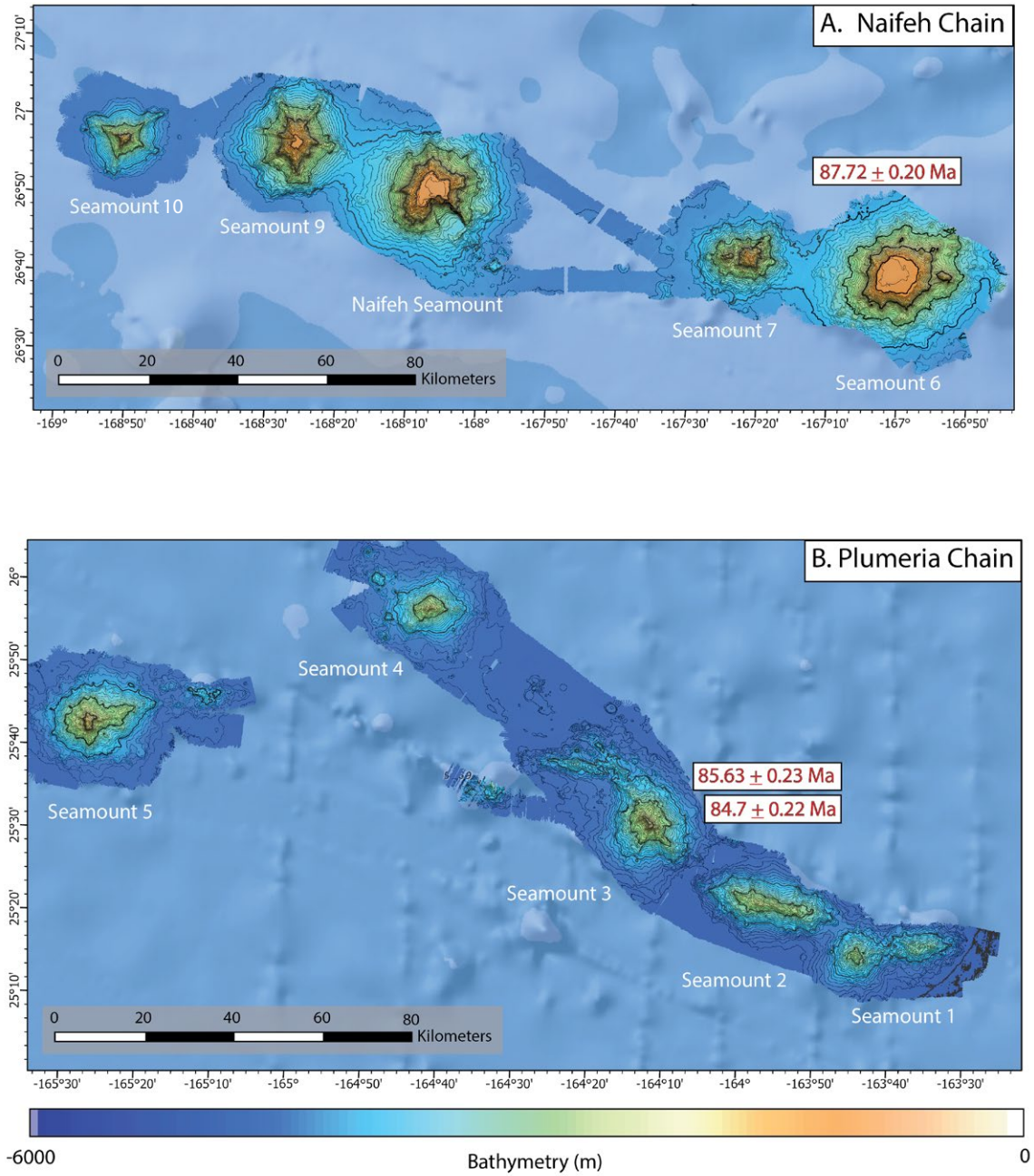

Figure 3. A 60-m-resolution bathymetric map shows the (A) Naifeh and (B) Plumeria chains. Contours are drawn at 100 m intervals. Color-scale bar indicates depth in meters below sea level (mbsl). Red text displays $^{40}Ar/^{39}Ar$ ages dated within the study (Table 1).

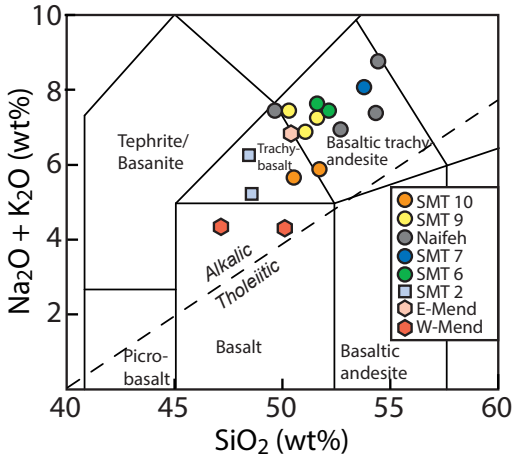

Figure 4. A total-alkali silica (TAS) diagram plots lava flow samples from the Naifeh and Plumeria chains (Montour et al., 2021; Pasqualon et al., 2022) as well as East Mendelssohn (E-Mend) and West Mendelssohn (W-Mend) (Pringle, 1992). All data represent whole-rock X-ray fluorescence spectrometry analyses. SMT—Seamount.

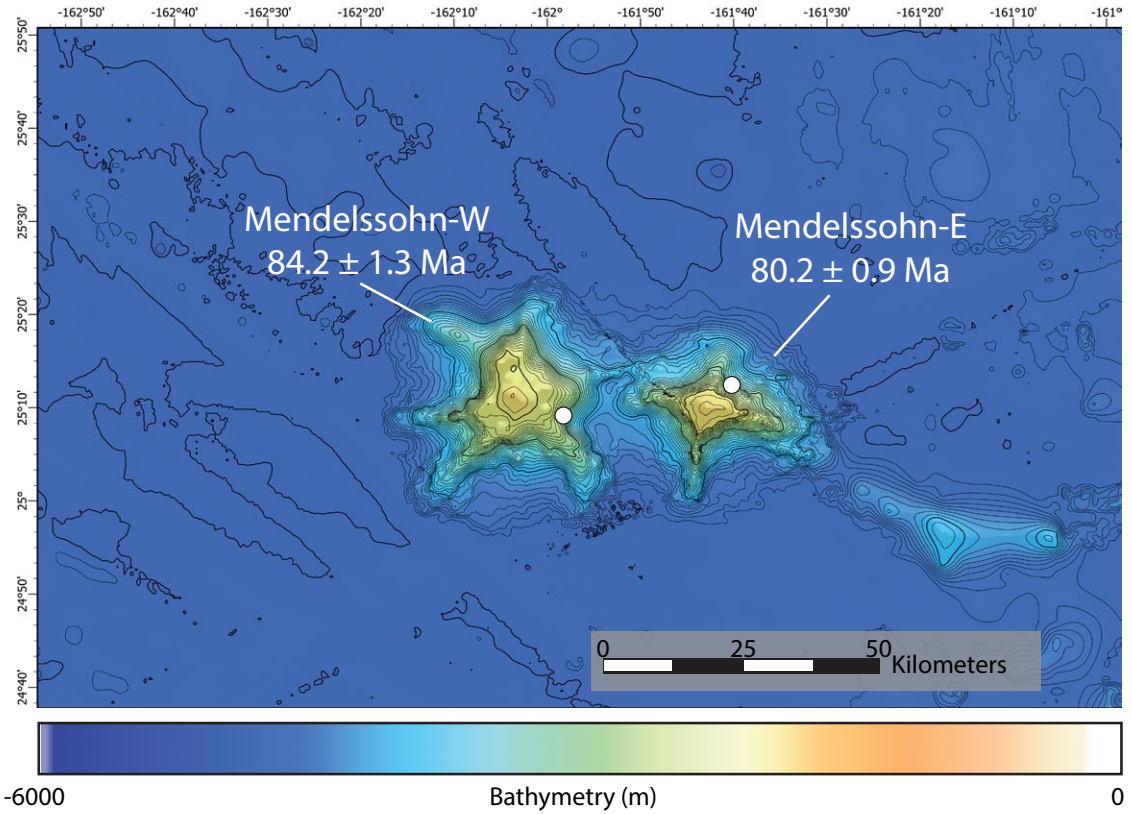

Figure 5. A bathymetric map shows the Mendelssohn Seamounts, which are composed of the Mendelssohn East and Mendelssohn West seamounts. The locations of two dredges are shown with white circles, and the corresponding $^{40}Ar/^{39}Ar$ ages are shown (Sager and Pringle, 1987).

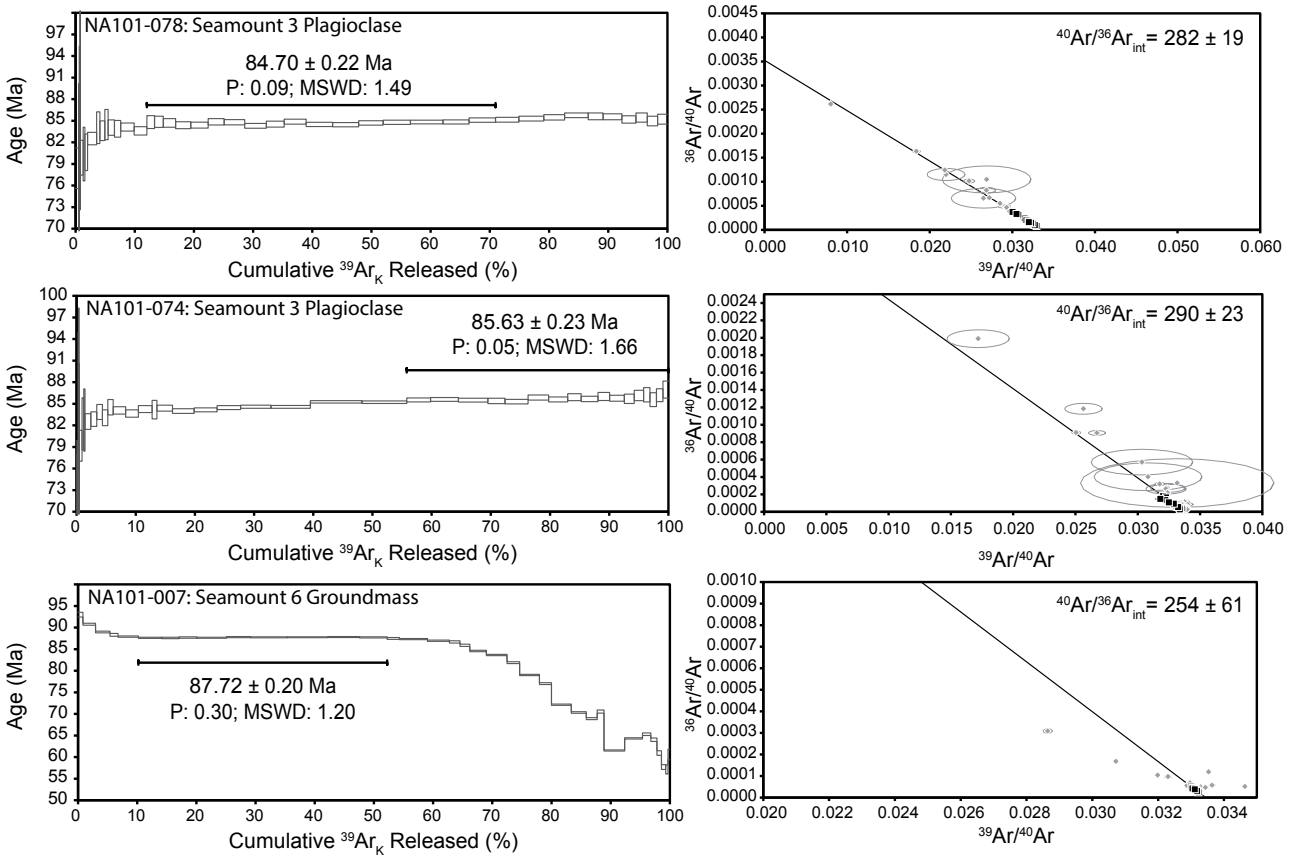

Figure 6. Incremental heating $^{40}Ar/^{39}Ar$ age-determination results are plotted. (Left) Age spectrums, where the line indicates the selected plateau region. MSWD—mean square of weighted deviates, P—probability of fit ($\chi 2$). (Right) Inverse isochron results with the selected plateau points (black) and unselected points (gray). All uncertainties are provided at the 2σ level.

TABLE 1. SUMMARY OF SUCCESSFUL $^{40}Ar/^{39}Ar$ AGE-DETERMINATION RESULTS

Seamount	Sample	Material	Plateau age (Ma)	±2σ (i)	^{39}Ar	$^{40}Ar/^{36}Ar$ intercept	±2σ	MSWD	P	n	N	Inverse isochron age (Ma)	± 2σ (i)
Seamount 3	NA101-074	Plagioclase	85.63	0.23	44%	290.15	22.68	1.49	9%	17	42	85.7	0.28
Seamount 3	NA101-078	Plagioclase	84.7	0.22	59%	281.87	18.90	1.66	5%	17	42	84.94	0.37
Seamount 6	NA101-007	Groundmass	87.72	0.20	42%	253.64	61.34	1.2	30%	9	36	87.86	0.29

Notes: MSWD—mean square of weighted deviates; P—probability of fit; n—steps used in the plateau calculation; N—total heating steps; i—internal uncertainty.

in discordant age spectrums (e.g., Jiang et al., 2021). In total, three samples produced age determinations with plateau ages containing at least 40% of the ^{39}Ar argon released (Table 1).

Except for NA101-007, all groundmass analyses, which are separates of the interstitial mesostasis between phenocrysts, produced similar degassing spectrums. These patterns start with low-temperature recoil patterns (typically high apparent ages) or alteration (lower apparent ages) followed by 5–15 concordant temperature steps (23–31% ^{39}Ar released), then are proceeded by an extended high-temperature excess/recoil pattern that shows incrementally lower apparent ages with each step. The high-temperature steps typically show linear inverse isochron trends with negative ^{36}Ar/^{40}Ar intercepts. These trends are dissimilar to typical recoil-induced isochrons that follow an atmospheric trend but offset toward higher ^{39}Ar/^{40}Ar values (e.g., Koppers et al., 2007). This lack of non-recoil isochron patterns—coupled with the extensive high temperature, continually decreasing apparent ages—indicate a mixture of excess mantle Ar and recoil effects producing the discordant results. The commonality of these groundmass incremental heating patterns within our data set is likely due to the nature of ROV sampling, which typically focuses on sampling the broken outer crust of pillow basalts that erupted under high hydrostatic pressure. These margins likely trapped magmatic argon within interstitial glass (e.g., Dickin and Halliday, 1995). Repeat analyses of the groundmass separates produce concordant spectrums and plateaus, including two groundmass separates with concordant mini plateaus (^{39}Ar = 25–40%; P >0.05), atmospheric intercepts, and ages of ca. 88 Ma (NA101-024; Naifeh Guyot) and ca. 84 Ma (NA101-068; Seamount 4, Plumeria Chain). While not statistically robust, these two ages strengthen our findings that the two seamounts dated in the Naifeh and Plumeria chains are Late Cretaceous and formed during similar time intervals. If these ages are largely inaccurate, then the strong age concordance between these and neighboring seamounts would be fortuitous. We conclude that their concordance supports a ca. 88 Ma age for some seamounts in the Naifeh Chain and ca. 85 Ma age for some seamounts in the Plumeria Chain; however, we cannot assess the full potential range of eruption ages among the chains with the current data set.

Morphology of the Naifeh and Plumeria Seamounts

Seamounts within the Naifeh and Plumeria chains fall into three morphological groups: (1) round, flat-topped "guyots"; (2) small, conical seamounts; and (3) narrow, linear steeply sloped ridges. Primary geomorphic seamount features revealed by the newly acquired multibeam bathymetry are shown in Table 2 and discussed in the Plumeria Chain and Naifeh Chain subsections below.

Plumeria Chain

The Plumeria Chain is a NW–SE-trending ridge composed of five semi-linear ridged seamounts of similar size, shape, and slope (Fig. 3B). The average length of these ridges ranges from 20 km to 30 km, with the overall chain spanning roughly 200 km.

Seamount 1: Seamount 1 (Fig. 7) is the easternmost seamount of the Plumeria Chain, which lies 240 km NE of Mokumanamana. It is an E–W-trending linear ridge connected to a radial seamount by a saddle. The combined length of these two features created a 28-km-long, E–W-trending, semi-linear ridge. The narrow linear ridge is characterized by the steep flanks of its north- and south-facing walls, which alternate in morphology between smooth and fluted. The linear ridge has an overall length of 13 km and a summit depth of ~3000 m below sea level (mbsl), with flanks displaying an average slope of between 14° and 19°. Rugged bathymetry of the lower half along the linear ridge is composed of sparsely scattered volcanic cones and a potential terrace that may represent tube-fed lava deltas. On the eastern side of the linear ridge, there is a circular depression, which may represent an unfilled

TABLE 2. GEOMORPHIC OBSERVATIONS OF THE MAPPED NAIFEH-PLUMERIA CHAIN SEAMOUNTS

Seamount	Latitude (°N)	Longitude (°W)	Area (km^2)	Depth to summit (mbsl)	Long axis length (km)	Morphology
Plumeria Chain						
Seamount 1	25.317	163.742	630	3000	13	Conical seamount connected to an E–W ridge
Seamount 2	25.403	163.925	760	2150	35	Linear E–W-oriented ridge
Seamount 3	25.555	164.202	1730	1800	19	Conical seamount with bifurcating W–NW-trending ridges
Seamount 4	25.972	164.745	930	2100	15	Semi-conical seamount
Seamount 5	25.696	165.469	1160	1600	25	Conical seamount with an eastward-projecting ridge
Naifeh Chain						
Seamount 6	26.704	166.987	1380	870	30	Conical guyot
Seamount 7	26.793	167.363	1070	1250	18	Conical seamount with a pronounced western ridge
Naifeh	26.853	168.066	1740	770	22	Conical guyot with large sector collapse
Seamount 9	27.029	168.495	1050	930	19	Conical guyot
Seamount 10	26.951	168.875	430	1490	17	Conical seamount

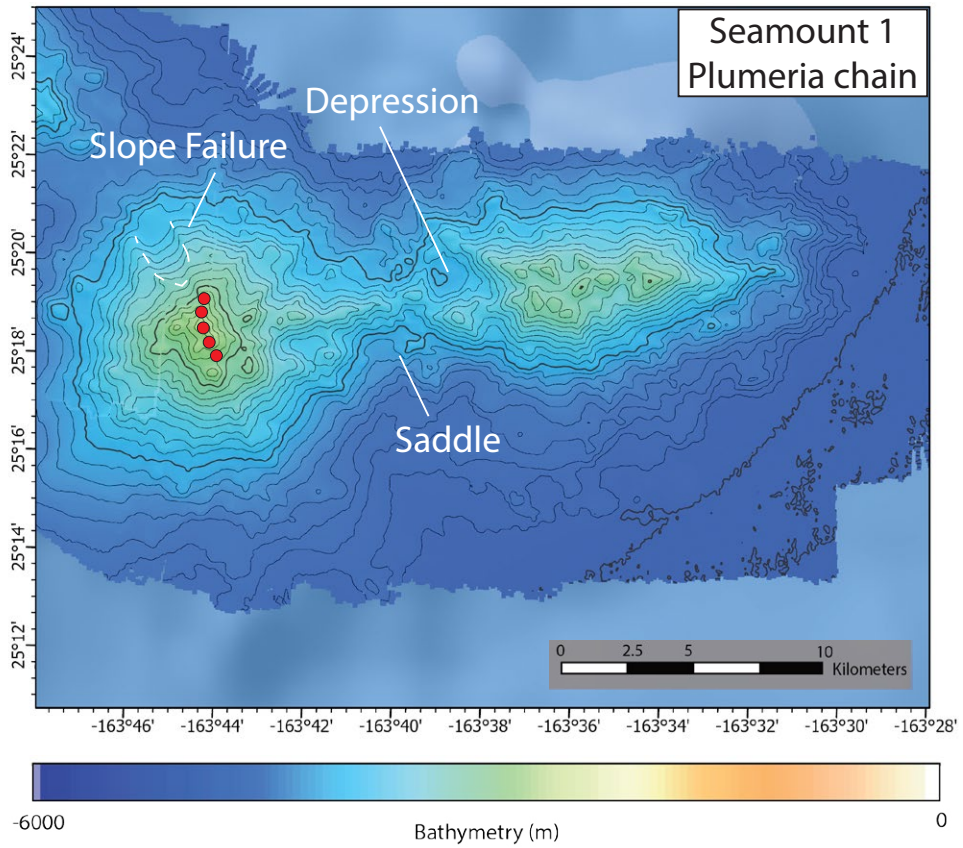

Figure 7. Color-shaded relief bathymetric map of Seamount 1 is shown. The contour interval is 100 m. The saddle between the two peaks combining the linear ridge and conical mass is noted. Red circles represent rock samples collected by the ROV *Hercules* on dive H1726.

caldera. The estimated height of the depression is 300 m from rim to base.

The adjacent semicircular conical edifice that lies west of the linear ridge and is connected by a saddle can be characterized by its broadly circular, rugged base, which increases in slope from 12° to 17° toward the summit. The 10 km circular cone has a summit depth of 2500 mbsl and is the largest feature of this seamount by volume. Surrounding the northwestern and southeastern base of the seamount is a series of lobate lava flows, which collectively create a rugged base. Along the southwestern side, shallower slopes of 5° at the base may result from slope failures. The northwestern portion of the seamount contains a scarp and sequential debris field, which are indicative of a slope failure (Fig. 7).

Two igneous rocks (NA101-104 and NA101-114) recovered were selected for age-determination analyses. The samples are from relatively deep depths on the ridge slope (2696 mbsl and 2794 mbsl). NA101-104 is a plagioclase-clinopyroxene alkali basalt with a fine-grained, pervasively altered groundmass and calcite amygdules. NA101-114 is a three-phase alkali basalt (plagioclase, olivine, and clinopyroxene) with similar fine-grained, pervasively altered groundmass and calcite amygdules. All olivine within lava flows recovered during NA101 had completely recrystallized to iddingsite. A plagioclase separate from NA101-104 displayed a disturbed age spectrum with two mini-plateaus (Supplemental Material [see footnote 1]). Conservatively, we did not assign an age to this sample. Plagioclase separated from NA101-114 produced a highly disturbed spectrum that is reminiscent of a mixture between recoil and excess Ar contamination.

Seamount 2: Seamount 2 (Fig. 8) lies ~3 km northwest of Seamount 1. Seamount 2 is partially connected to Seamount 1 by a slightly elevated rift zone, which is ~300 m higher than the abyssal seafloor. Seamount 2 is an E–W-trending, narrow linear ridge that is ~35 km long, and its summit depth is 2150 mbsl. The steep-sided edifice has an average slope that ranges from 16° to 18°. The northern and southern flanks of the linear ridge display a smooth, fluted morphology that is characterized by a couple of N–S-trending linear ridges similar to those of Seamount 1. Flank embayments appear to be present along this region, resulting in an accumulation of sediment at the base that creates a smoother slope. Slopes along the upper portion of the flank near the summit reach as high as 22° before shallowing. Along the southeastern side of the seamount, the slope shallows to <5°, creating a terrace area halfway up the seamount, which is then followed by a localized increase in slope of 21° off the edge of the terrace.

One igneous sample (NA101-099) recovered from 2407 mbsl was chosen for an age-determination experiment. Petrographic analyses indicate the sample is a plagioclase-olivine alkali basalt with a highly oxidized groundmass consisting primarily of plagioclase, magnetite, and olivine. A plagioclase separate produced a highly discordant age spectrum with at least four distinct "bursts" of excess argon (and corresponding high apparent ages) being released during the heating spectrum.

Seamount 3: Seamount 3 (Fig. 9), located ~8 km west of Seamount 2, has a composite morphology consisting of a circular conical edifice with two bifurcating west/northwest-projecting curvilinear

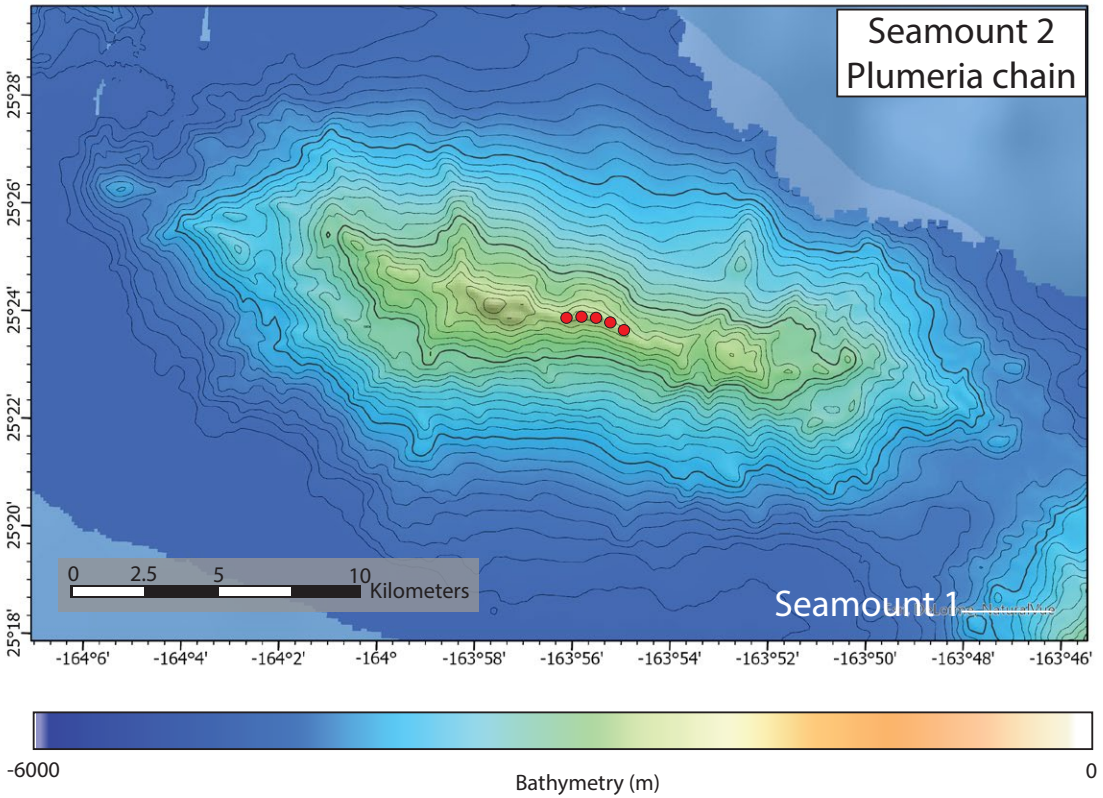

Figure 8. Color-shaded relief bathymetric map of Seamount 2 shows an E–W-trending linear ridge. A bridge partially connects Seamount 1 to Seamount 2 via elevated topography that is, on average, 300 m above the abyssal floor. The red circles represent samples collected by the ROV *Hercules* on dive H1725.

ridges, which collectively span a total length of ~39 km. The main semicircular conical edifice has a length of 18.5 km, width of 16 km, and a summit depth of ~1800 mbsl. Flanks along the main edifice have an average slope of 11°–13°. Localized variations exist along slope embayments along the northwestern and southern sides of the seamount that reach up to 22°. The western edges of the seamount display a smoother base that contrasts with the rugged base seen along the northern to northeastern sides.

Connected to the main circular edifice along the northwestern side of the seamount are two semilinear ridges that intersect prior to joining the main seamount structure. Ridge 1 has a length of ~21 km trending E–W and can be characterized by a series of connected circular volcanic cones with average summit depths of 3000 mbsl. The ridge slopes range from 18° to 20°.

Ridge 2 consists of one main ridge that is connected by elevated topography. Overall, the ridge spans 15 km and is characterized by steep flanks and lobate lava flows along the base, which create a rugged topography. Individual examples of these features vary in size up to a maximum diameter of ~3.5 km and a relief of ~500 m. Both projecting ridges are connected by a linear ridge at the northwestern side of the main edifice that measures roughly 6 km.

Two igneous samples were selected for age-determination experiments from this dive. Samples NA101-074 and NA101-078 were recovered from 1990 mbsl and 1955 mbsl, respectively. Sample NA101-074 is a plagioclase basalt with a pervasively oxidized holohyaline groundmass. A plagioclase separate from this lava produced a concordant mini-plateau (44% of ^{40}Ar released) with an age of 85.63 ± 0.23 Ma (Fig. 6). Sample NA101-078 is a plagioclase basalt with flow banding textures, with alteration varying significantly between layers. A plagioclase separate from this lava produced a concordant plateau with an age of 84.70 ± 0.22 Ma. The two age determinations are stratigraphically consistent and indicate that this seamount formed at ca. 85 Ma and was active for at least 1 Ma. Given the relatively close placement of the two lava flow samples, the seamount likely existed for much more than 1 Ma.

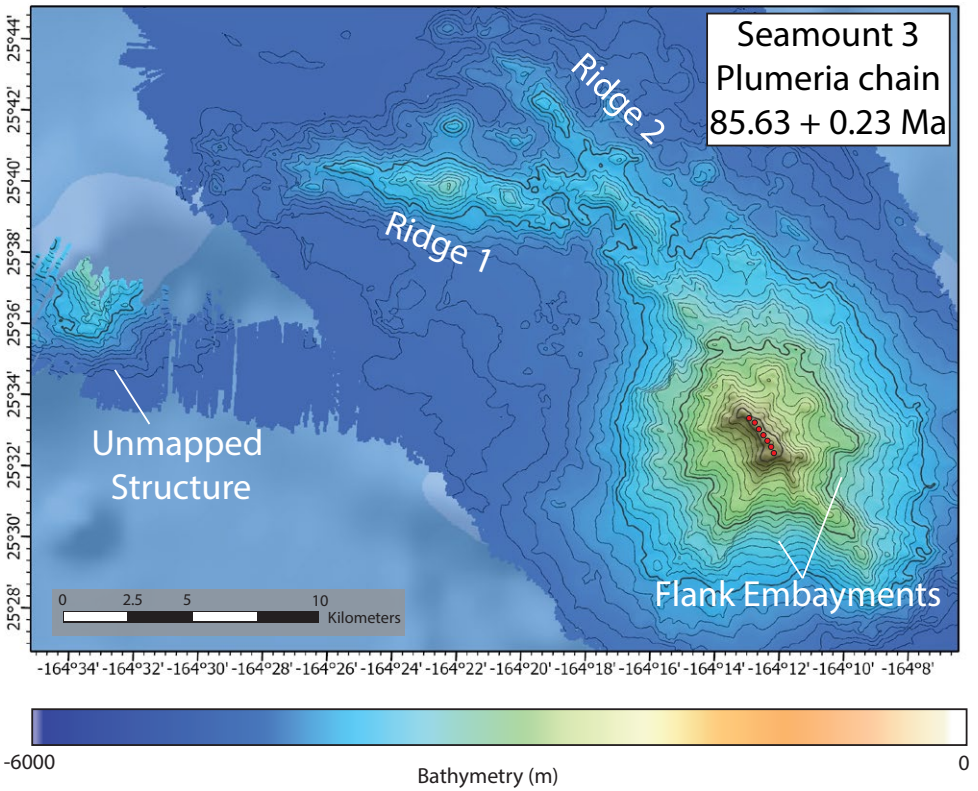

Figure 9. Color-shaded relief bathymetric map of Seamount 3 shows a conical edifice with two curvilinear ridges protruding to the west. A partially mapped structure exists to the west of the seamount. The red circles represent samples collected by the ROV *Hercules* on dive H1723.

Seamount 4: Seamount 4 (Fig. 10) lies 55 km (summit to summit) west of Seamount 3. The feature contains an oval base with sparse amounts of circular volcanic cones and mounds along the western and eastern edges of the seamount. The overall length of the seamount is ~15 km, with a summit depth of 2100 mbsl. Seamount 4 has an overall area of 9.3×10^6 km^2 and volume of 4.0×10^9 km^3, making it the smallest mapped seamount within the Plumeria Chain (Table 2). Semi-shallow flanks of 10–18° with a smooth texture surround the main edifice. The northeastern region of the seamount contains an apparent scarp with an ~30° slope, which is likely evidence of a slope failure.

Several mounds are observed off the western edge of the seamount. The largest mound can be characterized by a semicircular edifice with a 5-km-wide, shallow linear ridge extending off the eastern edge. Individual examples of these features vary in size up to a maximum diameter of 3 km and a height of 827 m relative to the surrounding seafloor. It is not apparent from the bathymetry whether these features formed in relation to the seamount or represent features intrinsic to the underlying crust.

Sample NA101-068 was recovered from 2351 mbsl and represents a plagioclase basalt with plagioclase phenocrysts showing a continual size spectrum from fine to microcrystic and phenocrystic. The sample contained relatively fresh groundmass with rare clinopyroxene microcrysts. A groundmass separate from the lava flow displayed a very short plateau (<40% ^{39}Ar released) at ca. 84 Ma, followed by an extensive recoil/excess pattern with decreasing apparent ages. A replicate analysis using a slightly different step-heating schedule produced the same (but slightly longer) plateau at ca. 84 Ma. Although the age is not statistically robust, the concordance with neighboring Seamount 3 lends some credibility that Seamount 4 was volcanically active in a similar time interval.

Seamount 5: Seamount 5 (Fig. 11) lies 55 km southwest of Seamount 4, 190 km northwest of Mokumanamana at Necker Seamount, and is the westernmost seamount along the Plumeria Chain. Multibeam bathymetry reveals a shield-shaped rugged base with evidence of a NE-trending linear ridge that contributes to the oval shape. Six kilometers east of the main edifice is a cluster of volcanic cones and mounds. The main edifice has a length of ~25 km and a summit depth of 1600 mbsl. Like the other structures in the Plumeria Chain, Seamount 5 has a multitude of radial ridges extending from its center. Flanks of the seamount have an average slope of ~17–19°, with localized increases in slope of ~23° along flank embayments. U-shaped slope channels have caused localized areas of increased sedimentation leading to changes in slope near the base. The overall rugged bathymetry of the lower half of the seamount is due to small, circular volcanic cones.

A smaller potential ridge system can be seen 6 km east of Seamount 5. This feature is composed of a series of small, circular, interconnected volcanic cones that resemble the same E–W-trending ridge seen from Seamount 5. This small structure has a length of 12 km and a summit depth of 3760 mbsl. Slopes vary between the structures but display an average angle of ~20°. All of the igneous samples recovered from the seamount were pervasively altered and lacked phenocryst phases and thus were not used for ^{40}Ar/^{39}Ar age-determination experiments.

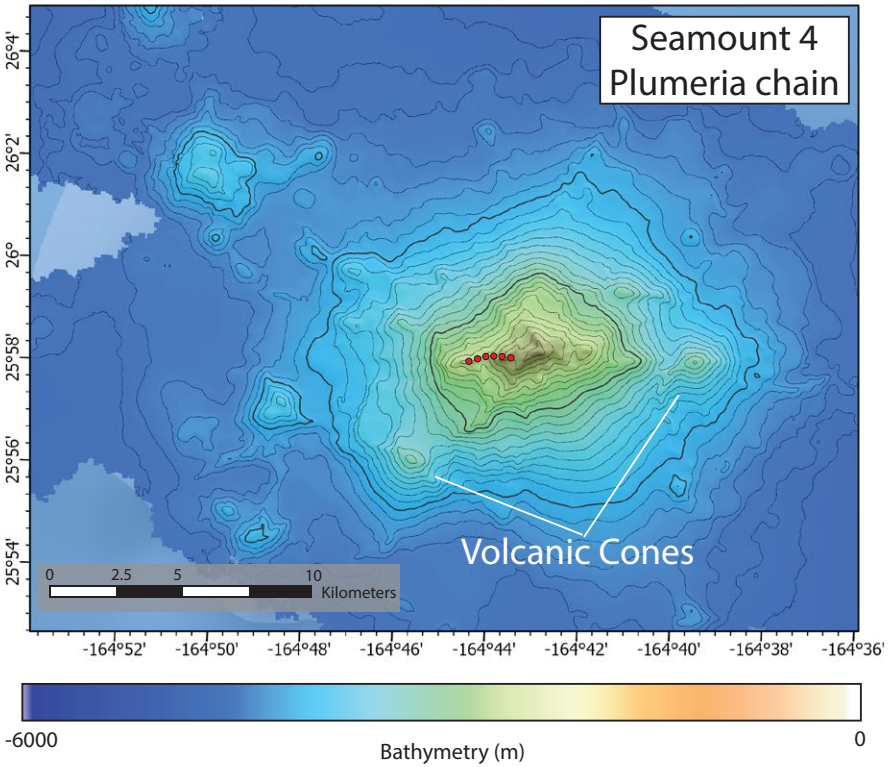

Figure 10. Color-shaded relief bathymetric map of Seamount 4 shows a conical edifice surrounded by lobate volcanic cones. Located to the NE of the seamount is a bathymetric high that may represent a satellite ridge or small volcanic cone. The red circles represent samples collected by the ROV *Hercules* on dive H1722.

Naifeh Chain

The Naifeh Chain is located ~100 km NW from Pūhāhonu and ~165 km west of the Plumeria Chain (Fig. 3A). The chain is composed of five conical, star-shaped seamounts, which span a total length of 220 km. Seamounts within the chain can be divided into two categories: guyots and star-shaped structures. Similar to the Plumeria Chain, the Naifeh Chain trends E–W between Seamount 6 in the east and Seamount 10 in the west. The Naifeh Chain is easily distinguishable from the Plumeria Chain by the difference in volume and area of the seamounts (Table 2). The Naifeh Chain overlies the Murray Fracture Zone and as such, it is possible that the relative size difference is a function of pre-existing lithospheric weaknesses providing more efficient conduits for melt ascension. In addition, the Naifeh Chain lies on the arch generated by Pūhāhonu, which accounts for shallowing of the local seafloor and seamounts relative to the Plumeria Chain.

Seamount 6: Seamount 6 (Fig. 12) is a guyot that lies ~105 km NW of the base of Pūhāhonu's northernmost point. The bathymetry includes a semicircular seamount with five main ridges extending out from the summit plateau. The guyot has a diameter of 30 km and a summit depth of 868 mbsl. The rugged bathymetry of the lower half of the seamount is composed of circular volcanic cones and craters, some of which have depths of ~10 m from peak to base.

Concentric rings at differing elevations on the central peak give a terrace appearance similar to what is observed in coastal environments during island subsidence (Simkin et al., 1972; Wilson et al., 1998). The overall length of the summit plateau is 11.2 km, making it the largest-diameter plateau of all the seamounts in the Naifeh Chain. The summit plateau has an average slope of <1°, which creates a flat surface. Two possible mechanisms could create this flat surfaced summit or guyot: (1) filling of a caldera, or (2) wave erosion during subsidence of an island (e.g., Simkin et al., 1972; Wilson et al., 1998; Chaytor et al., 2007).

The base of Seamount 6 contains several volcanic cones and flat-topped craters, some of which still exhibit a clear depression in the center. The average depths from rim to base of these craters are ~10 m. Individual examples of these volcanic cones vary in size up to a maximum diameter of 1.5 km and a height of 100–200 m. Most of these structures can be found at the base of the northeastern and southwestern sides of the seamount, where the average slopes of these volcanic cones range between 20° and 27°.

The flanks of Seamount 6 have an average slope of between 13° and 17°, with significant local variations along the extending ridges (up to 25°). The northeastern and southwestern flanks of the main edifice are more rugged than the northwestern and southeastern sides due to the presence of steep-sided linear ridges and a flank embayment. The base of the northeastern section of the seamount contains unorganized mounds, which are potentially indicative of debris from a slope failure or parasitic volcanic cones. In the northeast, two steep-sided ridges run approximately perpendicular to each other and attach at the summit plateau. The average slope between the two ridges ranges from 15° to 23°. The southwest is characterized by two smaller ridge systems that connect to the summit plateau. Along these ridges, the average slope ranges between 21° and 24°. Higher slopes are potentially the result of slope failure along the southern side of the seamount. The eastern side of

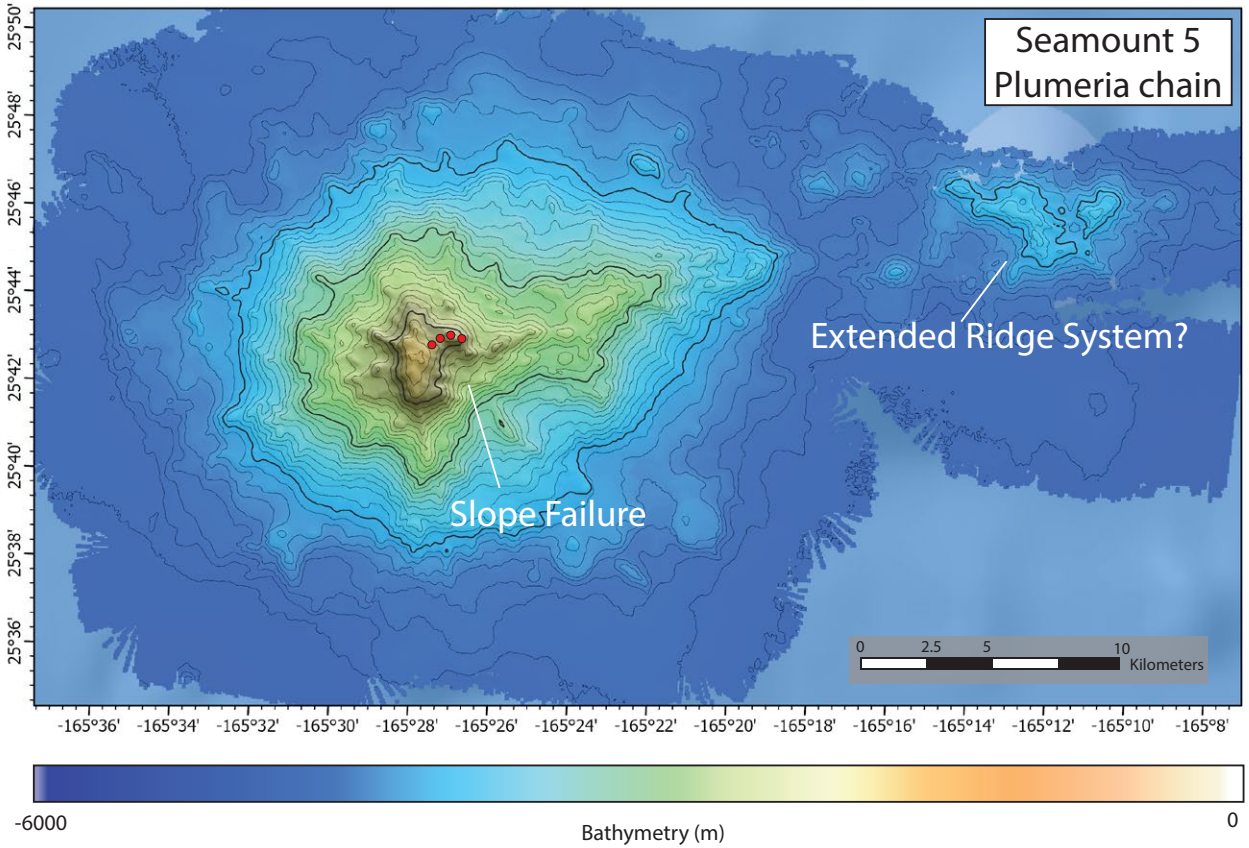

Figure 11. Color-shaded relief bathymetric map of Seamount 5 depicts a semi-conical main edifice. An extended ridge system, outlined in black, can be seen along the northwest. The red circles represent samples collected by the ROV *Hercules* on dive H1724.

the seamount represents a large, detached bathymetric high that may be either a secondary volcanic edifice or a large mass wasted block. This feature was the site of dive H1715.

Seamount 6 was explored twice (by dives H1715 and H1721), and age-determination experiments were carried out on the most suitable sample from each dive. NA101-007 is a plagioclase basalt with a holocrystalline groundmass texture recovered from 1580 mbsl. The plagioclase phenocrysts displayed very spongey textures and were deemed unsuitable for analysis. A groundmass separate produced a concordant mini-plateau (42% ^{39}Ar) with an age of 87.72 ± 0.20 Ma (Fig. 6). Sample NA101-056 was gathered at 2233 mbsl depth and is a plagioclase-olivine basalt. The groundmass contains trace olivine and plagioclase within a holohyaline mesostasis. A plagioclase separate produced a highly disturbed spectrum with discordant releases of excess magmatic ^{40}Ar at the mid–high temperature steps.

Seamount 7: Seamount 7 (Fig. 13) is located 16 km west of Seamount 6. The morphology of Seamount 7 is characterized by an oval-shaped base with two main edifices and radial ridges that extend outward from their centers. The edifices have depths of 1249 mbsl (east) and 2000 mbsl (west) and are separated by a saddle. The overall length of the E–W-trending seamount is ~18 km. The average slope angles of the main edifice range between 16° and 18°, with localized variances along the radiating volcanic ridges, which average 25–33°. Well-developed U-shape chutes are present on the northern and eastern flanks of Seamount 7, where an increase in the deposition of sediments has potentially smoothed out the base. A few

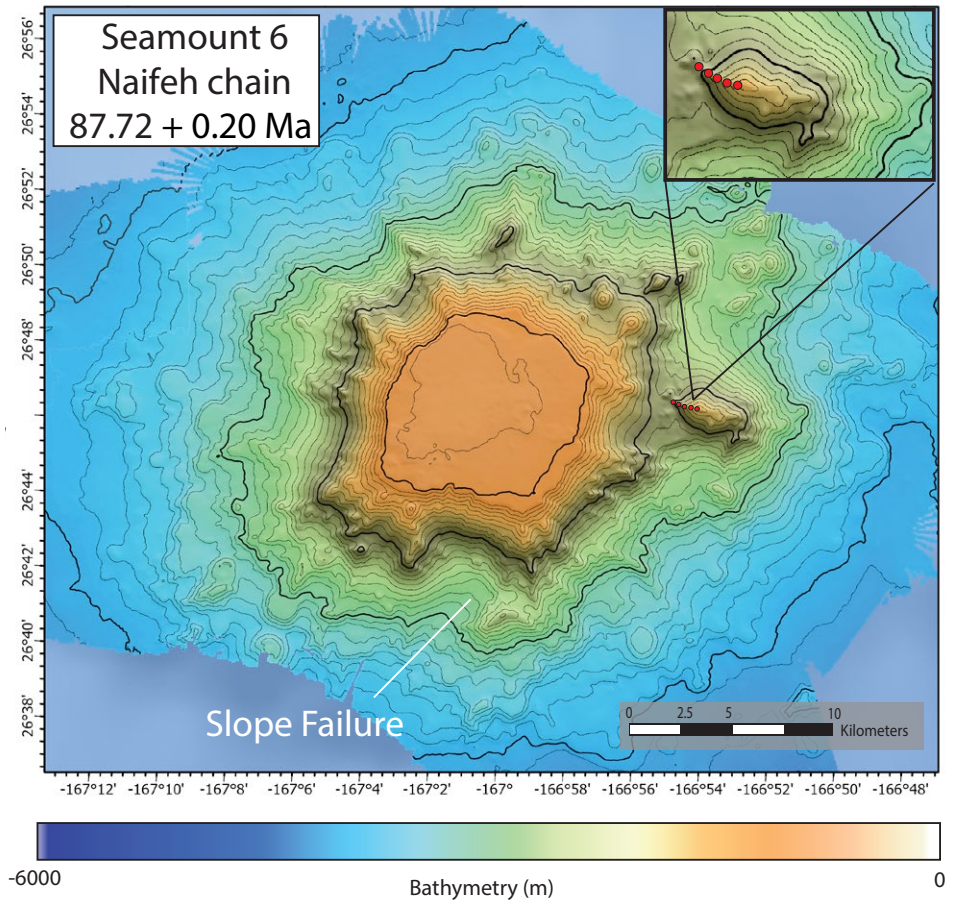

Figure 12. Color-shaded relief bathymetric map of Seamount 6 depicts a semi-conical guyot with five ridges extending out from the summit's plateau. The red circles represent samples collected by the ROV *Hercules* on dives H1715 and H1721. Satellite map in top right-hand corner magnifies the path taken by the rover.

sparse circular volcanic cones can be seen along the southeastern and southwestern edges of the seamount's base, which contributes to the rugosity along the base.

Sample NA101-012 was recovered from 1555 mbsl and is a plagioclase basalt with plagioclase phenocrysts and a single clinopyroxene phenocryst observed in the petrographic thin section. The groundmass consists of plagioclase microcrysts within a holohyaline textured mesostasis. The sample had both calcite amygdules and Fe hydroxide-rimmed vesicles. A plagioclase separate produced a discordant spectrum, likely resulting from a mixture of recoil, sericite alteration, and excess magmatic $^{40}Ar/^{36}Ar$.

Naifeh Guyot: Naifeh Guyot (Fig. 14) is located 50 km west of Seamount 7 and marks the approximate center of the Naifeh Chain. It is composed of a main flat plateau edifice with several smaller volcanic ridges extending from its center. The guyot contains a distinctive plateau summit with two to three steps that differ in elevation. As at Seamount 6, these stepped terraces may be indicative of costal processes from potential wave erosion along the surface (e.g., Simkin et al., 1972; Wilson et al., 1998). Accordingly, the stepped terraces dip away from the center slightly, with an average plateau slope of <3°. The length of the plateau is roughly 10 km with a width of 7 km. Several peaks ranging from 200 m to 400 m in length and 50 m to 100 m in height are found all along the summit plateau, which potentially indicate post-erosional volcanism. The overall length of the guyot is 22 km, with an edifice depth of 767 mbsl and a basal depth of 3760 mbsl, which make it the tallest seamount within both chains. The flanks of the guyot have an average slope of 17–25° along the main structure before shallowing out at the base. Significant local variations within the slope are observed along areas of failure, with the most prominent slope failure located on the southern side of the seamount, where slopes reach a maximum of 50°.

Five major ridge systems extend from the main plateau edifice outward, with lengths of up to 7 km. The majority of the ridges are NE–SW-trending and can be traced through the summit's plateau, with the exception of one major ridge in the northeast. In the SE, trending ridges run parallel to each other, creating a ridge-to-gully geometry. Flank embayment and U-shaped chutes along the western and southern flanks of the seamount have increased sedimentation, resulting in the appearance of a smoother base. Specifically, two linear scarp features along the southeastern flank of the seamount cut from the base to the summit to form a U-shaped embayment, which constitutes evidence of a massive sector collapse. Further evidence of failure can be seen on the abyssal seafloor, where considerable debris is accumulated.

Two samples from Naifeh Guyot were selected for $^{40}Ar/^{39}Ar$ age determinations. NA101-023 was an alkali basalt collected at 2201 mbsl. The lava flow was composed of a plagioclase–clinopyroxene–olivine basalt. The plagioclase and clinopyroxene phenocrysts were relatively unaltered. The

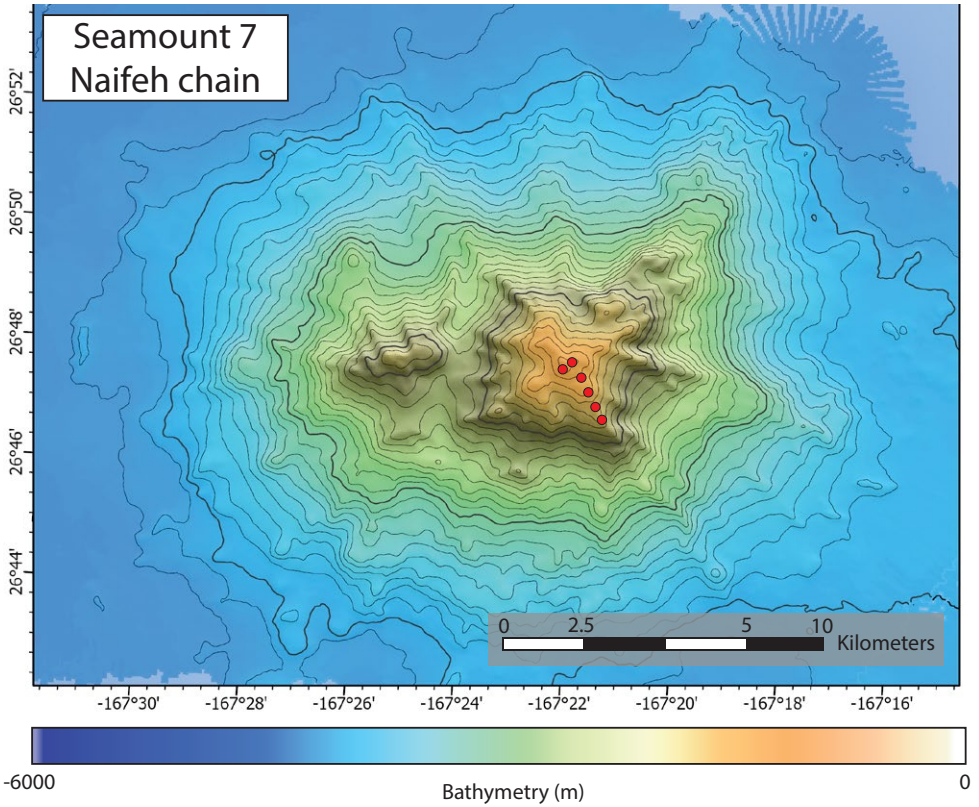

Figure 13. Color-shaded relief bathymetric map of Seamount 7 depicts a semi-conical main edifice with three main ridges extending out from the center. A second volcanic edifice is present to the east, separated by a saddle. The red circles represent samples collected by the ROV *Hercules* on dive H1716.

groundmass consists of plagioclase, olivine, clinopyroxene, and spinel in an oxidized, glassy mesostasis. A plagioclase separate produced a discordant plateau. Sample NA101-024 was recovered from 2171 mbsl. Petrographically, the sample is very similar to NA101-023, except the groundmass displays trachytic textures. Two groundmass step-heating experiments were undertaken, producing short (<40% ^{39}Ar), concordant plateaus at ca. 88 Ma.

Seamount 9: Seamount 9 (Fig. 15) is located 15 km west of Naifeh Guyot and contains a small plateaued summit, which indicates the feature is likely a guyot. The seamount displays a generally circular edifice with six narrow linear ridges radially extending from the summit. The seamount is characterized by its star-shaped morphology and has an overall length of 19 km. Seamount 9 has a flat plateau with a slope of <2° and a diameter of ~3 km. The seamount potentially contains a second terrace level with a steeper slope (>5°) that dips outward. On average, the plateau depth is 930 mbsl.

The flanks of the main edifice have an average slope of 16–21° near the plateau and are shallow toward the base. The shallowing of the slope may result from erosion and sedimentation, likely aided by U-shaped channels along a majority of the flanks. Localized variations with significant increases in slope are observed along the northeastern side of the seamount along the plateau. Here, over-steepened and smooth-textured flanks along ridge five near the plateau have a slope of ~30°, which is significantly steeper than the slope of the main edifice. A U-shaped channel is present on the northern side of the guyot.

An age determination was attempted for one lava flow sample from the seamount (NA101-050). The lava flow was a plagioclase basalt with fine-grained plagioclase laths in a pervasively oxidized glass matrix. A plagioclase separate from the sample produced a discordant heating spectra.

Seamount 10: Seamount 10 (Fig. 16) lies ~22 km west of Seamount 9 and is the westernmost structure in the Naifeh Chain. The seamount has a summit depth of 1488 mbsl. Seamount 10 can be characterized by its four distinctive, sharp, narrow ridges that radially extend from the center to create an overall star-shaped morphology. The average length of the seamount is ~17 km, with an overall area of 7.5×10^6 km^2 and a volume of 3.0×10^9 km^3 (Table 2). This makes it the smallest structure along the Naifeh Chain. The flanks of the main edifice have an average slope of 23°, with local variation along the ridges reaching a maximum slope of 27°. Minimal ruggedness is observed along this seamount, except for one small, circular volcanic cone protruding along the north-facing flank.

One age determination (NA101-043) was attempted on a lava flow recovered from 2228 mbsl. The lava flow is a holocrystalline aphyric basalt with plagioclase, clinopyroxene, olivine, and spinel, with some regions displaying pervasively oxidized holohyaline textures. A groundmass separate produced a discordant plateau that represents a mixture of partial degassing, recoil, and excess ^{40}Ar/^{36}Ar.

DISCUSSION

The Naifeh and Plumeria Seamount Chains

The Naifeh and Plumeria chains represent a mixture of low-volume ridges, submarine

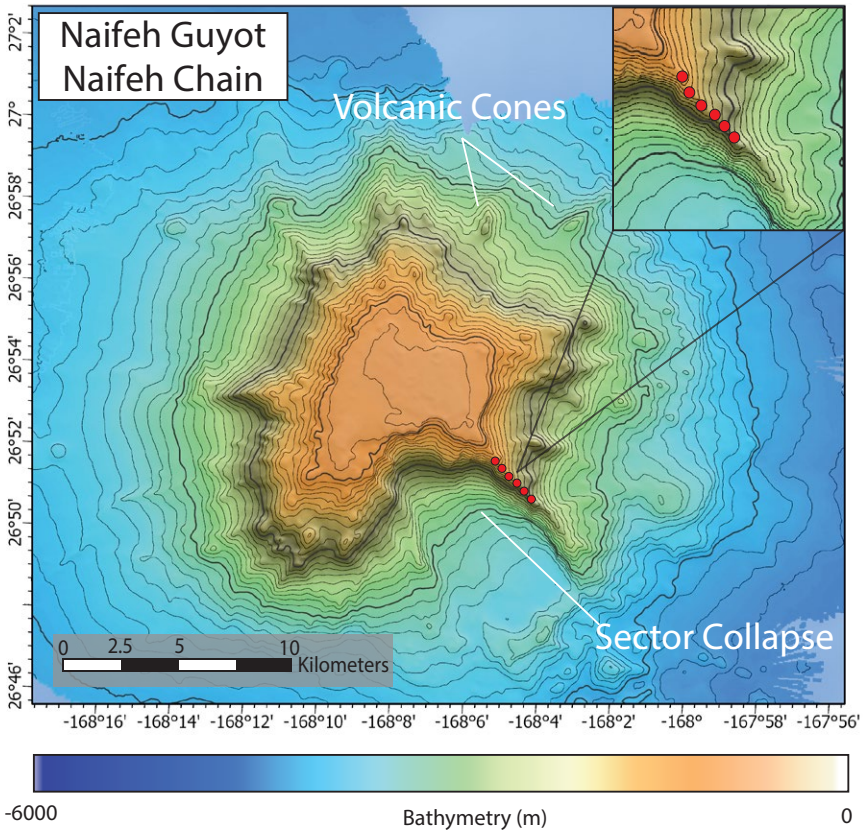

Figure 14. Color-shaded relief bathymetric map of Naifeh Guyot (Seamount 8) depicts a semi-conical main plateaued edifice with six ridges extending out from the guyot's center. The red circles represent samples collected on dive H1716. Satellite map in top right-hand corner magnifies the path taken by the ROV.

seamounts, and moderate-volume guyots that are composed of alkalic basalts. The Naifeh Chain contains larger-volume seamounts and guyots that formed at ca. 88 Ma, while the Plumeria Chain contains lower-volume seamounts and formed at ca. 85 Ma (Tables 1 and 2). The three guyots of the Naifeh Chain all have flat peaks at water depths of 0.8–0.9 km, which indicates they were likely subaerial at a similar time and were flattened by wave erosion during subsidence. In addition, we include the similarly orientated Mendelssohn Seamounts, which include two seamounts with 84 Ma (Mendelssohn West) and 80 Ma (Mendelssohn East) dredged lava flows (Fig. 5; Sager and Pringle, 1987; Pringle, 1992), in our discussion. In the following discussion sections, we discuss and test different formation mechanisms for the Naifeh–Plumeria–Mendelssohn chains considering the new data.

Arch Volcanism Origin

Arch volcanism is a geologic phenomenon that is hypothesized to be responsible for the unique volcanic features observed northwest and south of the Hawaiian Islands. In these areas, the South Arch (Lipman et al., 1989) and North Arch (Frey et al., 2000) volcanic fields lie on the Hawaiian Arch—a broad swell or bulge in the seafloor currently surrounding the active end of the Hawaiian Ridge. Although this arch volcanism represents a small volume compared to the volcanism of the main Hawaiian volcanoes, it spreads out over significant areas (>25,000 km^2; Frey et al., 2000). The most commonly suggested cause for the generation of arch magmas is flexing of the lithosphere under the weight (and loading) of the massive Hawaiian shield volcanic structures (e.g., Moore, 1970; Ten Brink and Brocher, 1987; Bianco et al., 2005). The Naifeh and Plumeria chains lie along the northern arch of the Northwestern Hawaiian Ridge (Fig. 2). Kelley et al. (2019) postulated that the Naifeh and Plumeria chains were formed from arch volcanic processes caused by the massive Pūhāhonu and Mokumanamana volcanoes (with ages of 15 Ma and 12 Ma; Garcia et al., 1987, 2015; Jicha et al., 2018). This hypothesis requires that the Naifeh and Plumeria chains formed contemporaneously with Pūhāhonu and Mokumanamana. The newly acquired Late Cretaceous ages for seamounts in the Naifeh and Plumeria chains eliminate the possibility of an arch volcanic origin.

Spreading Center or Intraplate Origin

Spreading centers with anomalous melt volume can produce seamounts on or proximal to the ridge (Niu and Batiza, 1991). These processes result in seamounts that generally are close in age to the underlying crust, low in volume compared to plume-derived seamounts, and form lineaments perpendicular to the spreading axis. It is difficult to determine the exact age of the oceanic crust underlying the Naifeh–Plumeria–Mendelssohn chains since it was formed during the Cretaceous Normal Superchron (C34n, 122–83 Ma; Granot et al., 2012). Models of the Pacific-Farallon spreading rate during the Cretaceous Superchron indicate that the crust beneath the Naifeh–Plumeria–Mendelssohn chains likely formed in the 100–90 Ma timeframe

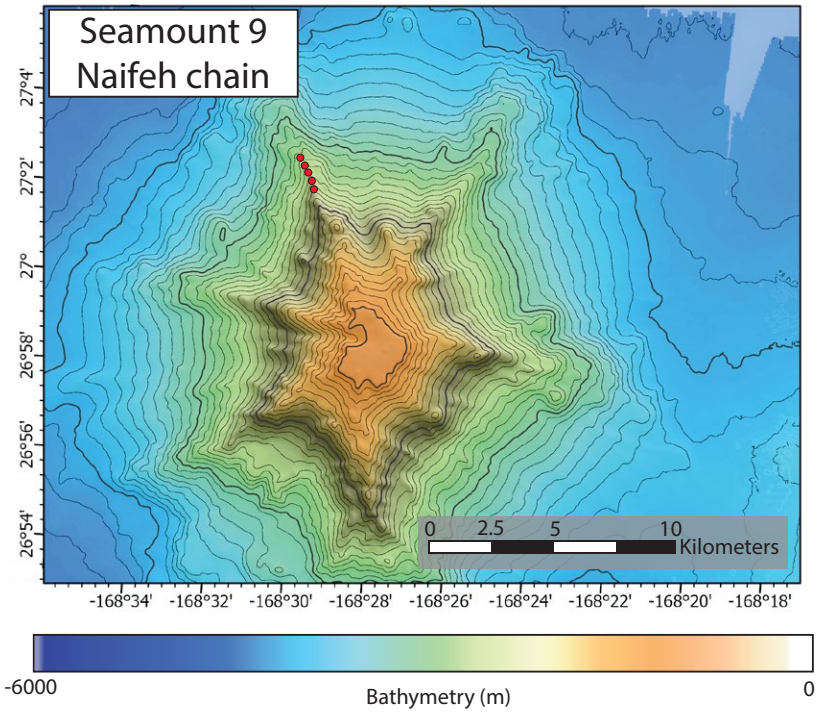

Figure 15. Color-shaded relief bathymetric map of Seamount 9 depicts a semi-conical guyot edifice with six ridges extending out from its center. The red circles represent samples collected by the ROV *Hercules* on dive H1718.

(Matthews et al., 2016). Given the fast ~50–60 mm/yr half-spreading rates modeled for the region (Müller et al., 2008), the Naifeh–Plumeria–Mendelssohn seamounts (88–80 Ma) would have formed ~500–900 km away from the ancient Pacific-Farallon Ridge. The combination of off-ridge volcanism and the alkaline nature of the basalts (Fig. 4) provide strong support for an intraplate volcanic origin.

Mantle-Plume Origin

Mantle plumes are large, thermochemical upwellings of deep mantle material that are fixed relative to the lithosphere (e.g., Koppers et al., 2021). As a consequence of their fixed nature, mantle plumes generate seamount chains that are age-progressive in the direction of plate motion. Absolute plate motion models of the Pacific during the Late Cretaceous indicate a general NW vector of motion (Duncan and Clague, 1985; Koppers et al., 2001; Wessel and Kroenke, 2008; Torsvik et al., 2019). However, the Naifeh and Plumeria chains have a west-to-east trend that is not compatible with an age-progressive NW–SE-orientated trend (Fig. 17), like the neighboring Wentworth Seamount (94–88 Ma; Pringle and Dalrymple, 1993) and Musician Seamount (98–76 Ma; Pringle, 1992) chains (Fig. 2). Independent plume motion (e.g., Steinberger, 2000; Konrad et al., 2018) could potentially account for the shape of the seamount chains. However, to accommodate the 88 Ma age of Seamount 6 and the 84 Ma age of Mendelssohn West would require eastward plume drift rates of ~12.5 cm yr^{-1}, which is significantly faster than what has been observed on Earth and only possible in extreme theoretical scenarios (Arnould et al., 2020). Therefore, a mantle-plume origin for these seamounts is highly improbable.

Lithospheric Extension Origin

Extension of the oceanic lithosphere can reduce the extent of local crustal loading through lithospheric thinning and allow for lower lithosphere/upper asthenosphere melts to ascend. One of the most argued examples of extension-derived volcanism on the Pacific plate is the Pukapuka Ridge system (18°S, 113.6°W to 14°S, 141.3°W) (Sandwell et al., 1995; Janney et al., 2000; Fig. 1). This represents a region of unusually enriched mantle and thin lithosphere with ridge and seamount chains that display no consistent age progressions (Sandwell et al., 1995; Janney et al., 2000). This region of the modern-day Pacific is potentially akin to the Naifeh–Plumeria–Mendelssohn chains, and as such, diffusive lithospheric extension provides a reasonable mechanism for generating the seamounts. Later research would argue for an asthenospheric shear origin for the Pukapuka Ridge, which is discussed further in the Shear-Driven Upwelling Origin subsection below. To get a pulse of lithospheric extension, a plate-driven mechanism is required that would provide tensional forces in the direction perpendicular to the orientation of the seamount chain. Although much of the northern regions of the Pacific Basin during the Late Cretaceous has been subducted beneath the Aleutian arc, evidence for the sudden establishment of new spreading centers at the Chinook Trough (Fig. 1) remain and provide circumstantial evidence for widespread regional extension.

Here, we propose a regional extensional model that reconciles the origin of the Naifeh–Plumeria–Mendelssohn chains in the ancient East Pacific. The 105 Ma global plate reorganization event (Matthews et al., 2012) resulted in a series of significant changes within the Pacific Basin that were ultimately related to the collision of the

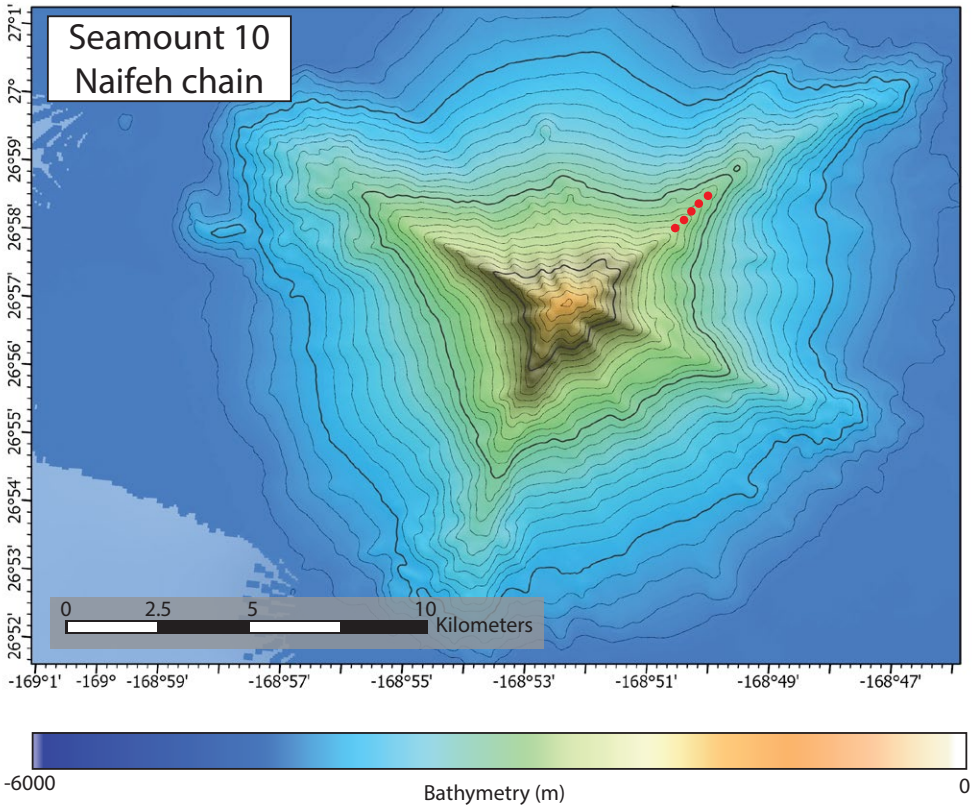

Figure 16. Color-shaded relief bathymetric map of Seamount 10 depicts a star-shaped seamount with four linear ridges protruding from the center peak. Smooth topography outlines the flanks and base of the seamount with the exception of one volcanic cone along the northern flank. The red circles represent samples collected by the ROV *Hercules* on dive H1718.

Hikurangi Plateau and the SE Gondwana margin (ca. 110–100 Ma). The collision caused subduction to cease and was followed by the cessation of spreading within the Ellice Basin and Osbourn paleo-spreading centers and resulted in the joining of the Manihiki and Hikurangi plates onto the Pacific plate (e.g., Worthington et al., 2006; Mortimer et al., 2019; Torsvik et al., 2019). The exact timing of these events is not well constrained since they occurred during the Cretaceous Normal Superchron (C34n, 122–84 Ma; Granot et al., 2012). Mortimer et al. (2019) showed that a pulse of non-age–progressive intraplate volcanism on and around Chatham Rise (currently SW Pacific; Fig. 1) occurred between 99 Ma and 78 Ma (yellow stars; Fig. 18). This volcanism overlaps with the non-plume–derived intraplate volcanism found within the Naifeh–Plumeria–Mendelssohn chains (88–80 Ma; Fig. 2). The choking of the SE Gondwana subduction zone, followed by the termination of spreading at the Osbourn Trough and Ellice Basin, occurred while subduction of the Izanagi plate beneath the North American and Eurasian plates continued (e.g., Seton et al., 2012). We speculate that the continued subduction in the north Pacific Basin—while plate boundaries were reconfigured in the south Pacific Basin—would gradually increase ~N–S extensional strain along the eastern Pacific plate over millions of years. During this time period, the Naifeh–Plumeria–Mendelssohn chains could have formed from lithospheric thinning. Once extensional strain exceeded the load that could be accommodated through crustal deformation, new spreading ridges formed to alleviate the tension along the Pacific plate. At 84–79 Ma, the Pacific-Kula spreading ridge developed north of the Naifeh–Plumeria–Mendelssohn chains (e.g., Lonsdale, 1988; Atwater, 1989; Norton, 2007; Seton et al., 2012). This timing is evident from magnetic isochrons north of the Chinook Trough that progress northward from C34n to C24r and younger at the Aleutian Trench (Atwater, 1989). The spreading center that generated this crust, as well as remnants of the eastern Izanagi plate during the Late Cretaceous, have since been subducted, which complicates our understanding of the Kula plate origin. Engebretson et al. (1985) postulated that the Kula-Pacific spreading initiated due to the cessation of spreading between the Pacific and Izanagi plates resulting in an eastward jumping of the spreading center. However, Seton et al. (2012) argued that the spreading between the Kula–Pacific–Farallon plates occurred while Izanagi-Pacific spreading was ongoing, and a triple junction initiated at or slightly before 79 Ma (C33r). Although no clear driving force for the initiation of the Kula-Pacific spreading is known, it is highly improbable that a new spreading center and plate would develop when the Pacific Basin had geodynamically stable plate configurations. As such, the shared timing of the initiation of Kula-Pacific spreading at 84–79 Ma (Atwater, 1989; Seton et al., 2012) and the apparent ceasing of parallel volcanism among the Naifeh–Plumeria–Mendelssohn chains at ca. 80 Ma imply a shared relationship. Most importantly, similar wide-spread, low-volume deformation volcanism preceded the opening of the Pacific-Antarctic Ridge at the same time (ca. 84 Ma; Mortimer et al., 2019). Thus, we postulate that lithospheric extension could have driven intraplate volcanism along the Naifeh–Plumeria–Mendelssohn chains until the initiation of the Kula-Pacific spreading ridge alleviated the regional tension.

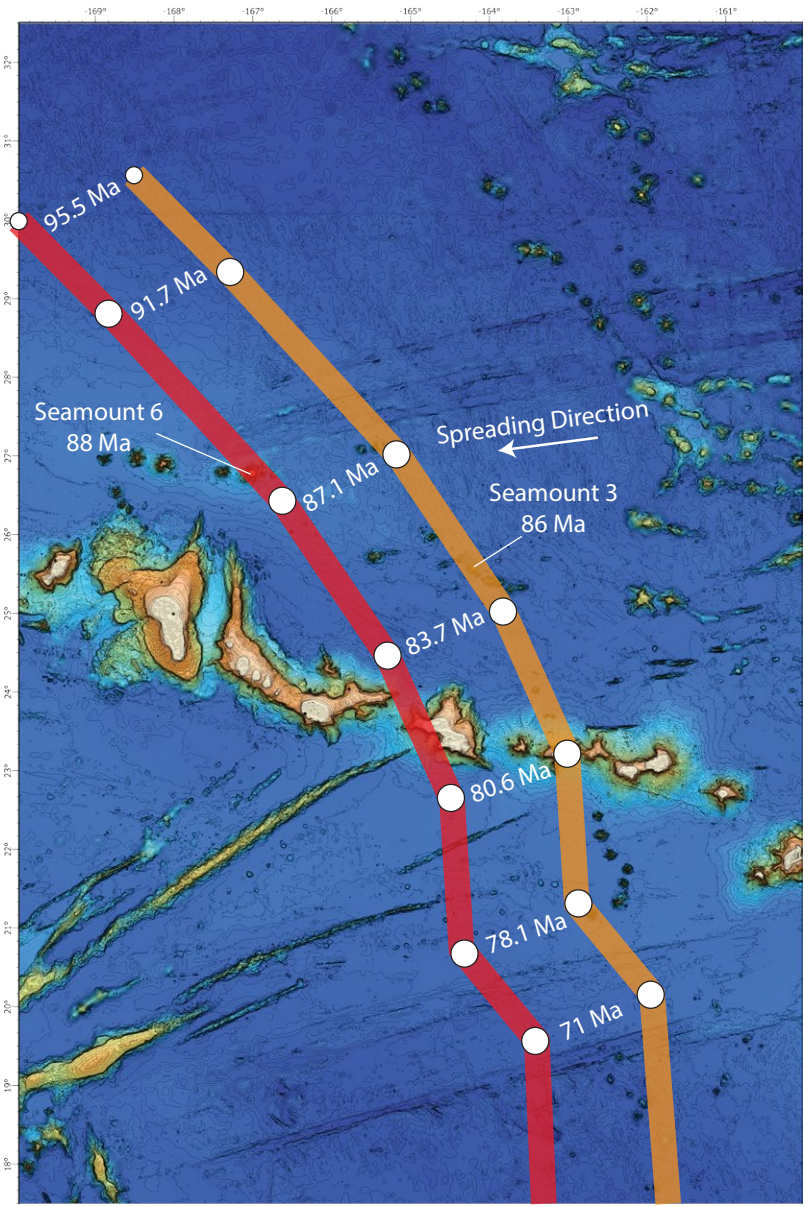

Figure 17. A bathymetric map of the study region with superimposed modeled hotspot tracks constructed with the ages and locations of Seamount 6 (red) and Seamount 3 (orange) uses the absolute plate motion model of Wessel and Kroenke (2008). Note that neither the Naifeh nor Plumeria chains match the expected geometry and age progressions of a fixed hotspot track.

Shear-Driven Upwelling Origin

Near-ridge asthenospheric shear-driven upwelling (SDU) in regions of enriched mantle can potentially produce intraplate volcanism with rough age-progressions that are more consistent with spreading rates and not absolute plate motion (Ballmer et al., 2013). Asthenospheric shear occurs when the large-scale flow of the asthenosphere operates in an opposite direction from lithospheric movement due to crustal growth and spreading (e.g., Conder et al., 2002; Conrad et al., 2011). Comparisons between modeled asthenospheric flow vectors from seismically derived mantle density anomalies and plate motions indicate that the region immediately west of the East Pacific Rise has the highest potential for shear-related volcanism today (Conrad et al., 2011). In addition, shear was found to be greatest on seafloor that is less than 10 Ma. This has led Conrad et al. (2011) to argue for an SDU origin for many of the low-volume intraplate seamounts near the East Pacific Rise, including the Pukapuka Ridge. Ballmer et al. (2013) further examined the role of SDU west of the East Pacific Rise and indicated that low-viscosity fingers can be entrained away from spreading centers and melt at their apex, upwards of hundreds of kilometers away from the spreading axis. The asthenospheric shear intensity models rely on seismic tomographic imaging of the modern mantle (e.g., Conrad et al., 2011), and thus back-calculating flow into the Cretaceous is unreliable. However, the similarity in features of the Naifeh–Plumeria–Mendelssohn chains and low-volume intraplate volcanism near the East Pacific Rise support a potential SDU origin for the seamounts we studied.

The Naifeh–Plumeria–Mendelssohn chains display the following characteristics that are consistent with SDU related volcanism. (1) The Naifeh–Plumeria–Mendelssohn chains orientations are slightly oblique to the paleo-spreading axis (albeit not perpendicular as models predict; Ballmer et al., 2013), and they formed on young crust within 1000 km of the ridge axis. (2) The seamounts are all low-volume and primarily (or entirely) composed of alkali basalts (including Mendelssohn; Sager and Pringle, 1987). (3) The available age determinations

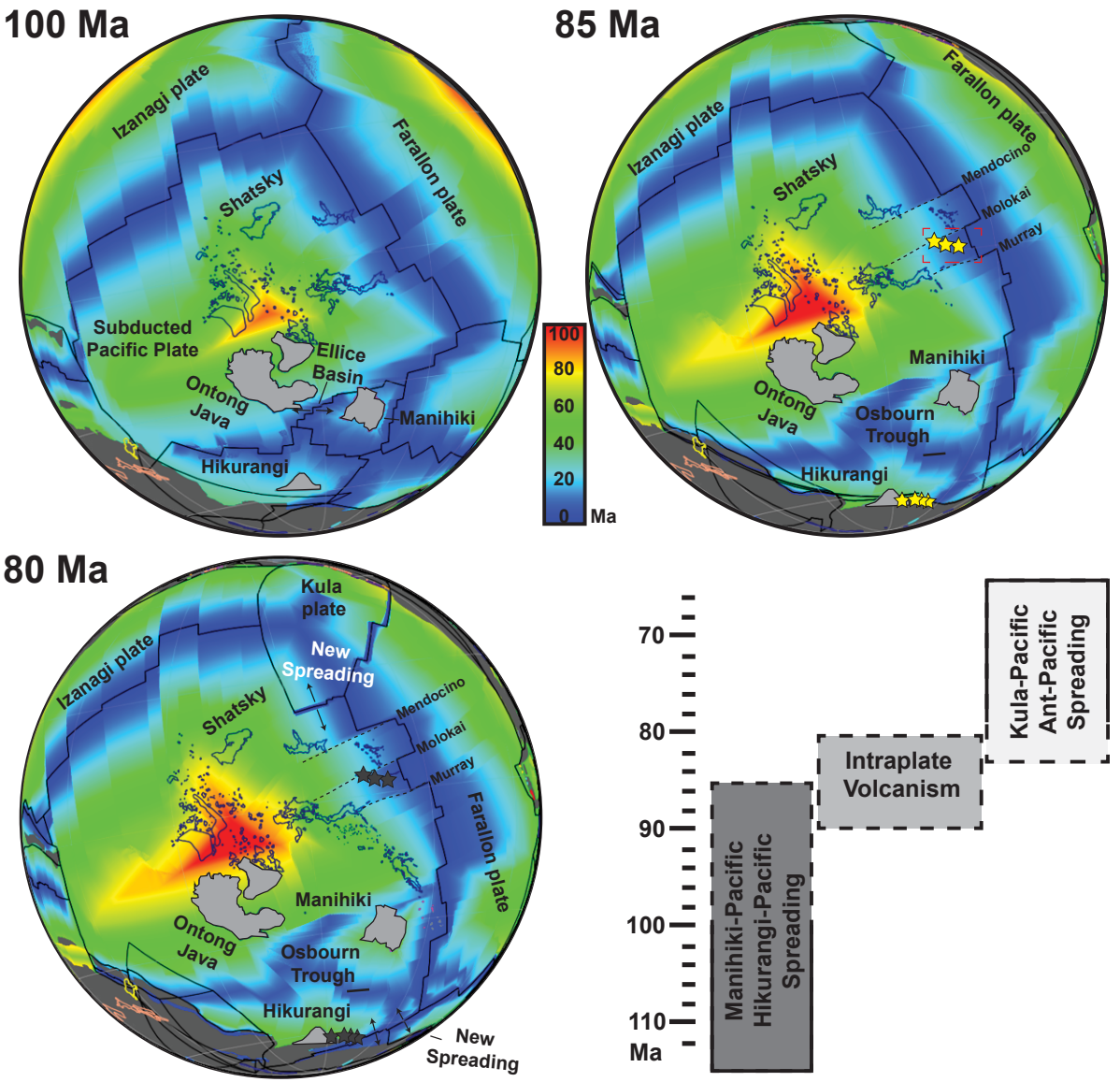

Figure 18. Reconstructions of the Pacific and surrounding plates during the 100 Ma, 85 Ma, and 80 Ma timeframes are based on the models of Müller et al. (2019) and Torsvik et al. (2019). The color shading represents the crustal age at the time step shown (given in Ma). Ontong Java and its separated plateaus are shown with gray shading for reference. Yellow stars indicate regions of active deformation-derived intraplate volcanism during the 85 Ma timeframe, while black stars represent their apparent inactivity at 80 Ma. Red dashed box indicates area of study (Naifeh–Plumeria–Mendelssohn chains). A scale bar indicating the timing of microplate cessation is shown, with solid lines for the 95 Ma age proposed in Mortimer et al. (2019) and dashed lines for the 86 Ma age proposed in Torsvik et al. (2019).

indicate a rough age progression of the chains from the westmost Seamount 6 (88 Ma) to Seamount 3 (86–85 Ma) to Mendelssohn West (84 Ma) to the easternmost Mendelssohn East (80 Ma; Fig. 2). This rough age progression is in the direction of crustal spreading as opposed to plate motion (Fig. 17). (4) The viscous fingers likely require some degree of heterogeneously enriched mantle (low-viscosity pockets; Ballmer et al., 2013), which in the case of the Naifeh–Plumeria–Mendelssohn chains, could be derived from the Euterpe Hotspot that ascended near the Pacific-Farallon spreading center at the time the Naifeh–Plumeria–Mendelssohn chains formed (Pringle, 1992; Kopp et al., 2003; O'Connor et al., 2015). Given these observations, an SDU origin is plausible for the Naifeh–Plumeria–Mendelssohn chains. Further research is warranted that incorporates geochemical constraints and additional successful age determinations to see if the chain is truly age progressive and chemically compatible with the melting of low-viscosity asthenospheric pockets or, alternatively, if extensional deformation is a better explanation for the origin of these seamounts.

CONCLUSIONS

Here, we provide new high-resolution bathymetry, coupled with geochronological data of pillow basalt lava flows recovered from ridges along previously unexplored seamounts from the Naifeh and Plumeria chains of the North Pacific. Each chain is composed of five mapped seamounts separated by ~170 km. The Plumeria Chain has a more E–W-trending ridge-like structure with overall smaller seamount volumes relative to the Naifeh Chain, which contains three guyots. New geochronological data from the seamounts reveal Late Cretaceous-aged pillow basalts from the Naifeh and Plumeria chains. The $^{40}Ar/^{39}Ar$ age determinations indicate a ca. 88 Ma age for Seamount 6 in the Naifeh Chain and a ca. 85 Ma age for Seamount 3 in the Plumeria Chain. By reconciling new ages and geomorphological indicators with similar regional volcanic structures and tectonic events, we conclude that:

(1) The Late Cretaceous-aged seamounts in the Naifeh and Plumeria chains are inconsistent with Hawaiian Arch volcanism and on-ridge spreading processes.

(2) The orientation and age of the Naifeh and Plumeria chains relative to the Pacific plate motion indicate that a mantle-plume origin is unlikely.

(3) The Naifeh–Plumeria–Mendelssohn chains appear to be similar in origin to the younger Pukapuka Ridge, which is found in the south Pacific. Therefore, we propose that either shear-driven upwelling or plate extension is responsible for the origin of the chains.

ACKNOWLEDGMENTS

We thank the captain and crew of the *E/V Nautilus* during expedition NA101. Daniel Heaton is thanked for his assistance in handling the $^{40}Ar/^{39}Ar$ age determinations. We thank Natalia Pasqualon for providing the whole rock X-ray fluorescence spectrometry data. We thank QPS for providing license access to Qimera and Fledermaus software. Funding for the expedition was from a NOAA Office of Exploration and Research grant (NA17OAR0110336) to the Ocean Exploration Trust. Activities were permitted under a research permit (PMNM 2018-027) from the Papahānaumokuākea Marine National Monument, U.S. Fish and Wildlife Service, and the Department of the Interior. A. Balbas and A. Sotomayor were supported by National Science Foundation–Division of Ocean Sciences (NSF-OCE) grant 1936544, J.G. Konter was supported by NSF-OCE grant 1936453, and V.D. Wanless was supported by NSF-OCE grant 1936461.

REFERENCES CITED

Arnould, M., Coltice, N., Flament, N., and Mallard, C., 2020, Plate tectonics and mantle controls on plume dynamics: Earth and Planetary Science Letters, v. 547, https://doi.org/10.1016/j.epsl.2020.116439.

Atwater, T., 1989, Plate tectonic history of the northeast Pacific and western North America, *in* Winterer, E.L., Hussong, D.M., and Decker, R.W., eds., The Eastern Pacific Ocean and Hawaii: Boulder, Colorado, Geological Society of America, Geology of North America, v. N, p. 21–70, https://doi.org/10.1130/DNAG-GNA-N.21.

Balbas, A., Koppers, A.A., Kent, D.V., Konrad, K., and Clark, P.U., 2016, Identification of the short-lived Santa Rosa geomagnetic excursion in lavas on Floreana Island (Galapagos) by $^{40}Ar/^{39}Ar$ geochronology: Geology, v. 44, p. 359–362, https://doi.org/10.1130/G37569.1.

Ballmer, M.D., Conrad, C.P., Smith, E.I., and Harmon, N., 2013, Non-hotspot volcano chains produced by migration of shear-driven upwelling toward the East Pacific Rise: Geology, v. 41, p. 479–482, https://doi.org/10.1130/G33804.1.

Bianco, T.A., Ito, G., Becker, J.M., and Garcia, M.O., 2005, Secondary Hawaiian volcanism formed by flexural arch decompression: Geochemistry, Geophysics, Geosystems, v. 6, https://doi.org/10.1029/2005GC000945.

Castillo, P.R., Clague, D.A., Davis, A.S., and Lonsdale, P.F., 2010, Petrogenesis of Davidson Seamount lavas and its implications for fossil spreading center and intraplate magmatism in the eastern Pacific: Geochemistry, Geophysics, Geosystems, v. 11, no. 2, https://doi.org/10.1029/2009GC002992.

Chaytor, J.D., Keller, R.A., Duncan, R.A., and Dziak, R.P., 2007, Seamount morphology in the Bowie and Cobb hot spot trails, Gulf of Alaska: Geochemistry, Geophysics, Geosystems, v. 8, no. 9, https://doi.org/10.1029/2007GC001712.

Conder, J.A., Forsyth, D.W., and Parmentier, E.M., 2002, Asthenospheric flow and asymmetry of the East Pacific Rise, MELT area: Journal of Geophysical Research: Solid Earth, v. 107, no. B12, p. ETG 8-1–ETG 8-13.

Conrad, C.P., Wu, B., Smith, E.I., Bianco, T.A., and Tibbetts, A., 2010, Shear-driven upwelling induced by lateral viscosity variations and asthenospheric shear: A mechanism for intraplate volcanism: Physics of the Earth and Planetary Interiors, v. 178, no. 3–4, p. 162–175, https://doi.org/10.1016/j.pepi.2009.10.001.

Conrad, C.P., Bianco, T.A., Smith, E.I., and Wessel, P., 2011, Patterns of intraplate volcanism controlled by asthenospheric shear: Nature Geoscience, v. 4, p. 317–321, https://doi.org/10.1038/ngeo1111.

Davis, A.S., Gray, L.B., Clague, D.A., and Hein, J.R., 2002, The Line Islands revisited: New $^{40}Ar/^{39}Ar$ geochronologic evidence for episodes of volcanism due to lithospheric extension: Geochemistry, Geophysics, Geosystems, v. 3, no. 3, p. 1–28, https://doi.org/10.1029/2001GC000190.

Davis, A.S., Clague, D.A., Paduan, J.B., Cousens, B.L., and Huard, J., 2010, Origin of volcanic seamounts at the continental margin of California related to changes in plate margins: Geochemistry, Geophysics, Geosystems, v. 11, no. 5, https://doi.org/10.1029/2010GC003064.

Dickin, A.P., and Halliday, A.N., 1995, Radiogenic Isotope Geology: Economic Geology and the Bulletin of the Society of Economic Geologists, v. 90, p. 2099–2099.

Duncan, R., and Clague, D., 1985, Pacific plate motion recorded by linear volcanic chains, *in* Nairn, A.E.M., Stehli, F.G., and Uyeda, S., eds., The Ocean Basins and Margins: Springer, v. 7A, p. 89–121, https://doi.org/10.1007/978-1-4613-2351-8_3.

Duncan, R.A., and Clague, D.A., 1985, Pacific plate motion recorded by linear volcanic chains, *in* Nairn, A.E.M., Stehli, F.G., and Uyeda, S., eds., The Ocean Basins and Margins: New York, Plenum, v. 7A, p. 89–121, https://doi.org/10.1007/978-1-4613-2351-8_3.

Engebretson, D.C., Cox, A., and Gordon, R.G., 1985, Relative Motions between Oceanic and Continental Plates in the Pacific Basin: Geological Society of America Special Paper 206, 60 p., https://doi.org/10.1130/SPE206.

Frey, F.A., Clague, D., Mahoney, J.J., and Sinton, J.M., 2000, Volcanism at the edge of the Hawaiian plume: Petrogenesis of submarine alkalic lavas from the North Arch volcanic field: Journal of Petrology, v. 41, p. 667–691, https://doi.org/10.1093/petrology/41.5.667.

Garcia, M.O., Grooms, D.G., and Naughton, J.J., 1987, Petrology and geochronology of volcanic rocks from seamounts along and near the Hawaiian Ridge: Implications for propagation rate of the ridge: Lithos, v. 20, p. 323–336, https://doi.org/10.1016/S0024-4937(87)80005-1.

Garcia, M.O., Smith, J.R., Tree, J.P., Weis, D., Harrison, L., and Jicha, B.R., 2015, Petrology, geochemistry, and ages of lavas from Northwest Hawaiian Ridge volcanoes, *in* Neal, C.R.,

Sager, W.W., Sano, T., and Erba, D., eds., The Origin, Evolution, and Environmental Impact of Oceanic Large Igneous Provinces: Geological Society of America Special Paper 511, p. 1–25, https://doi.org/10.1130/2015.2511(01).

Granot, R., Dyment, J., and Gallet, Y., 2012, Geomagnetic field variability during the Cretaceous Normal Superchron: Nature Geoscience, v. 5, p. 220–223, https://doi.org/10.1038/ngeo1404.

Hirano, N., Takahashi, E., Yamamoto, J., Abe, N., Ingle, S.P., Kaneoka, I., Hirata, T., Kimura, J.I., Ishii, T., Ogawa, Y., and Machida, S., 2006, Volcanism in response to plate flexure: Science, v. 313, 5792, p. 1426–1428, https://doi.org/10.1126/science.1128235.

Hoernle, K., White, J.D.L., van den Bogaard, P., Hauff, F., Coombs, D.S., Werner, R., Timm, C., Garbe-Schönberg, D., Reay, A., and Cooper, A.F., 2006, Cenozoic intraplate volcanism on New Zealand: Upwelling induced by lithospheric removal: Earth and Planetary Science Letters, v. 248, p. 350–367, https://doi.org/10.1016/j.epsl.2006.06.001.

Janney, P.E., Macdougall, J.D., Natland, J.H., and Lynch, M.A., 2000, Geochemical evidence from the Pukapuka volcanic ridge system for a shallow enriched mantle domain beneath the South Pacific Superswell: Earth and Planetary Science Letters, v. 181, p. 47–60, https://doi.org/10.1016/S0012-821X(00)00181-3.

Jiang, Q., Jourdan, F., Olierook, H.K.H., Merle, R.E., Verati, C., and Mayers, C., 2021, $^{40}Ar/^{39}Ar$ dating of basaltic rocks and the pitfalls of plagioclase alteration: Geochimica et Cosmochimica Acta, v. 314, p. 334–357, https://doi.org/10.1016/j.gca.2021.08.016.

Jicha, B.R., Garcia, M.O., and Wessel, P., 2018, Mid-Cenozoic Pacific Plate motion change: Implications for the Northwest Hawaiian Ridge and circum-Pacific: Geology, v. 46, p. 939–942, https://doi.org/10.1130/G45175.1.

Kelley, C., Hourigan, T., Raineault, N., Balbas, A., Wanless, D., Marsh, L., Wipfler, R., Ardor Bellucci, L., and Kane, R., 2019, Enigmatic seamounts: Exploring the geologic origins and biological communities in Papahānaumokuākea Marine National Monument: Oceanography, v. 32, https://doi.org/10.5670/oceanog.2019.supplement.01.

Kelley, S., 2002, Excess argon in K–Ar and Ar–Ar geochronology: Chemical Geology, v. 188, no. 1–2, p. 1–22, https://doi.org/10.1016/S0009-2541(02)00064-5.

King, S.D., and Anderson, D.L., 1998, Edge-driven convection: Earth and Planetary Science Letters, v. 160, p. 289–296, https://doi.org/10.1016/S0012-821X(98)00089-2.

Konrad, K., Koppers, A.A.P., Steinberger, B., Finlayson, V.A., Konter, J.G., and Jackson, M.G., 2018, On the relative motions of long-lived Pacific mantle plumes: Nature Communications, v. 9, 854, https://doi.org/10.1038/s41467-018-03277-x.

Konter, J.G., and Jackson, M.G., 2012, Large volumes of rejuvenated volcanism in Samoa: Evidence supporting a tectonic influence on late-stage volcanism: Geochemistry, Geophysics, Geosystems, v. 13, no. 6, https://doi.org/10.1029/2011GC003974.

Kopp, H., Kopp, C., Phipps Morgan, J., Flueh, E.R., Weinrebe, W., and Morgan, W.J., 2003, Fossil hot spot-ridge interaction in the Musicians Seamount Province: Geophysical investigations of hot spot volcanism at volcanic elongated ridges: Journal of Geophysical Research: Solid Earth, v. 108, https://doi.org/10.1029/2002JB002015.

Koppers, A.A.P., 2002, ArArCALC—software for $^{40}Ar/^{39}Ar$ age calculations: Computers & Geosciences, v. 28, p. 605–619, https://doi.org/10.1016/S0098-3004(01)00095-4.

Koppers, A.A.P., Morgan, J.P., Morgan, J.W., and Staudigel, H., 2001, Testing the fixed hotspot hypothesis using $^{40}Ar/^{39}Ar$ age progressions along seamount trails: Earth and Planetary Science Letters, v. 185, p. 237–252, https://doi.org/10.1016/S0012-821X(00)00387-3.

Koppers, A.A.P., Staudigel, H., Phipps Morgan, J., and Duncan, R.A., 2007, Nonlinear $^{40}Ar/^{39}Ar$ age systematics along the Gilbert Ridge and Tokelau Seamount Trail and the timing of the Hawaii-Emperor Bend: Geochemistry, Geophysics, Geosystems, v. 8, https://doi.org/10.1029/2006GC001489.

Koppers, A.A.P., Becker, T.W., Jackson, M.G., Konrad, K., Müller, R.D., Romanowicz, B., Steinberger, B., and Whittaker, J.M., 2021, Mantle plumes and their role in Earth processes: Nature Reviews Earth & Environment, v. 2, p. 382–401, https://doi.org/10.1038/s43017-021-00168-6.

Kuiper, K.F., Deino, A., Hilgen, F., Krijgsman, W., Renne, P., and Wijbrans, J.R., 2008, Synchronizing rock clocks of Earth history: Science, v. 320, p. 500–504, https://doi.org/10.1126/science.1154339.

Lipman, P.W., Clague, D.A., Moore, J.G., and Holcomb, R.T., 1989, South Arch volcanic field—Newly identified young lava flows on the sea floor south of the Hawaiian Ridge: Geology, v. 17, p. 611–614, https://doi.org/10.1130/0091-7613(1989)017<0611:SAVFNI>2.3.CO;2.

Lonsdale, P., 1988, Paleogene history of the Kula Plate: Offshore evidence and onshore implications: Geological Society of America Bulletin, v. 100, p. 733–754, https://doi.org/10.1130/0016-7606(1988)100<0733:PHOTKP>2.3.CO;2.

Matthews, K.J., Seton, M., and Müller, R.D., 2012, A global-scale plate reorganization event at 105–100 Ma: Earth and Planetary Science Letters, v. 355–356, p. 283–298, https://doi.org/10.1016/j.epsl.2012.08.023.

Matthews, K.J., Maloney, K.T., Zahirovic, S., Williams, S.E., Seton, M., and Mueller, R.D., 2016, Global plate boundary evolution and kinematics since the late Paleozoic: Global and Planetary Change, v. 146, p. 226–250, https://doi.org/10.1016/j.gloplacha.2016.10.002.

McKenzie, D., and Bickle, M.J., 1988, The volume and composition of melt generated by extension of the lithosphere: Journal of Petrology, v. 29, p. 625–679, https://doi.org/10.1093/petrology/29.3.625.

Min, K., Mundil, R., Renne, P.R., and Ludwig, K.R., 2000, A test for systematic errors in $^{40}Ar/^{39}Ar$ geochronology through comparison with U/Pb analysis of a 1.1-Ga rhyolite: Geochimica et Cosmochimica Acta, v. 64, p. 73–98, https://doi.org/10.1016/S0016-7037(99)00204-5.

Montour, G., Wanless, V.D., Balbas, A., Konter, J., Schwartz, D., Raineault, N., and Kelley, C., 2021, Investigating geochemical diversity of seamounts adjacent to the main Hawaiian–Emperor Seamount Chain: Insights into the petrogenesis of the Naifeh and un-named Seamounts: Abstract DI25B-0026 presented at 2021 Fall Meeting, AGU, New Orleans, Louisiana, 13–17 December.

Moore, J.G., 1970, Relationship between subsidence and volcanic load, Hawaii: Bulletin Volcanologique, v. 34, p. 562–576, https://doi.org/10.1007/BF02596771.

Morgan, W.J., 1972, Deep mantle convection plumes and plate motions 1: AAPG Bulletin, v. 56, p. 203–213, https://doi.org/10.1306/819A3E50-16C5-11D7-8645000102C1865D.

Mortimer, N., van den Bogaard, P., Hoernle, K., Timm, C., Gans, P.B., Werner, R., and Riefstahl, F., 2019, Late Cretaceous oceanic plate reorganization and the breakup of Zealandia and Gondwana: Gondwana Research, v. 65, p. 31–42, https://doi.org/10.1016/j.gr.2018.07.010.

Müller, R.D., Sdrolias, M., Gaina, C., and Roest, W.R., 2008, Age, spreading rates, and spreading asymmetry of the world's ocean crust: Geochemistry, Geophysics, Geosystems, v. 9, https://doi.org/10.1029/2007GC001743.

Müller, R.D., Zahirovic, S., Williams, S.E., Cannon, J., Seton, M., Bower, D.J., Tetley, M.G., Heine, C., Le Breton, E., Liu, S., and Russell, S.H., 2019, A global plate model including lithospheric deformation along major rifts and orogens since the Triassic: Tectonics, v. 38, no. 6, p. 1884–1907, https://doi.org/10.1029/2018TC005462.

Niu, Y., and Batiza, R., 1991, An empirical method for calculating melt compositions produced beneath mid-ocean ridges: Application for axis and off-axis (seamounts) melting: Journal of Geophysical Research: Solid Earth, v. 96, p. 21,753–21,777, https://doi.org/10.1029/91JB01933.

Norton, I.O., 2007, Speculations on Cretaceous tectonic history of the northwest Pacific and a tectonic origin for the Hawaii hotspot, *in* Fouler, G.R., and Jordan, D.M., Plates, Plumes and Planetary Processes: Geological Society of America Special Paper 430, p. 451–470, https://doi.org/10.1130/2007.2430(22).

O'Connor, J.M., Hoernle, K., Müller, R.D., Morgan, J.P., Butterworth, N.P., Hauff, F., Sandwell, D.T., Jokat, W., Wijbrans, J.R., and Stoffers, P., 2015, Deformation-related volcanism in the Pacific Ocean linked to the Hawaiian–Emperor Bend: Nature Geoscience, v. 8, p. 393–397, https://doi.org/10.1038/ngeo2416.

Pasqualon, N.G., Konter, J.G., Wanless, D., Balbas, A., and Cunningham, M.J., 2022, Exploring the origin of the Enigmatic Seamounts: Insights from geochemical and isotopic signatures [abs.]: Goldschmidt Conference Abstracts.

Pringle, M.S., and Dalrymple, G.B., 1993, Geochronological constrains on a possible hot spot origin for Hess Rise and the Wentworth Seamount chain, *in* Pringle, M.S., Sager, W.W., Sliter, W.V., and Stein, S., eds., The Mesozoic Pacific: Geology, Tectonics, and Volcanism: Washington, D.C., American Geophysical Union, Geophysical Monograph 77, p. 263–277, https://doi.org/10.1029/GM077p0263.

Pringle, M.S.J., 1992, Geochronology and petrology of the Musicians Seamounts, and the search for hot spot volcanism in the Cretaceous Pacific [Ph.D. thesis]: Honolulu, Hawaii, University of Hawaii at Mānoa.

Sager, W.W., and Pringle, M.S., 1987, Paleomagnetic constraints on the origin and evolution of the Musicians and South Hawaiian seamounts, Central Pacific Ocean, *in* Keating, B.H., Fryer, P., Batiza, P., and Boehlert, G.W., eds., Seamounts, Islands, and Atolls: Washington, D.C., American Geophysical Union, Geophysical Monograph 43, p. 133–162, https://doi.org/10.1029/GM043p0133.

Sandwell, D.T., Winterer, E.L., Mammerickx, J., Duncan, R.A., Lynch, M.A., Levitt, D.A., and Johnson, C.L., 1995, Evidence for diffuse extension of the Pacific Plate from Pukapuka ridges and cross-grain gravity lineations: Journal of Geophysical Research: Solid Earth, v. 100, p. 15,087–15,099, https://doi.org/10.1029/95JB00156.

Seton, M., Müller, R.D., Zahirovic, S., Gaina, C., Torsvik, T., Shephard, G., Talsma, A., Gurnis, M., Turner, M., Maus, S., and Chandler, M., 2012, Global continental and ocean basin

reconstructions since 200 Ma: Earth Science Reviews, v. 113, no. 3–4, p. 212–270.

Simkin, T., Shagam, R., Hargraves, R.B., Morgan, W.J., Van Houton, F.B., Burk, C.A., Holland, H.D., and Hollister, L.C., 1972, Origin of some flat-topped volcanoes and guyots, *in* Shagam, R., et al., eds., Studies in Earth and Space Sciences: Geological Society of America Memoir 132, p. 183–194, https://doi.org/10.1130/MEM132-p183.

Steinberger, B., 2000, Plumes in a convecting mantle: Models and observations for individual hotspots: Journal of Geophysical Research: Solid Earth, v. 105, p. 11,127–11,152, https://doi.org/10.1029/1999JB900398.

Steinberger, B., Sutherland, R., and O'Connell, R.J., 2004, Prediction of Emperor-Hawaii seamount locations from a revised model of global plate motion and mantle flow: Nature, v. 430, 6996, p. 167–173, https://doi.org/10.1038/nature02660.

Ten Brink, U.S., and Brocher, T.M., 1987, Multichannel seismic evidence for a subcrustal intrusive complex under Oahu and a model for Hawaiian volcanism: Journal of Geophysical Research: Solid Earth, v. 92, p. 13,687–13,707, https://doi.org/10.1029/JB092iB13p13687.

Torsvik, T.H., Steinberger, B., Shephard, G.E., Doubrovine, P.V., Gaina, C., Domeier, M., Conrad, C.P., and Sager, W.W., 2019, Pacific-Panthalassic reconstructions: Overview, errata and the way forward: Geochemistry, Geophysics, Geosystems, v. 20, p. 3659–3689, https://doi.org/10.1029/2019GC008402.

Weatherall, P., Marks, K.M., Jakobsson, M., Schmitt, T., Tani, S., Arndt, J.E., Rovere, M., Chayes, D., Ferrini, V., and Wigley, R., 2015, A new digital bathymetric model of the world's oceans: Earth and Space Science, v. 2, p. 331–345, https://doi.org/10.1002/2015EA000107.

Wessel, P., and Kroenke, L.W., 2008, Pacific absolute plate motion since 145 Ma: An assessment of the fixed hot spot hypothesis: Journal of Geophysical Research: Solid Earth, v. 113, https://doi.org/10.1029/2007JB005499.

Wessel, P., Sandwell, D.T., and Kim, S.-S., 2010, The global seamount census: Oceanography, v. 23, p. 24–33, https://doi.org/10.5670/oceanog.2010.60.

Wilson, P.A., Jenkyns, H.C., Elderfield, H., and Larson, R.L., 1998, The paradox of drowned carbonate platforms and the origin of Cretaceous Pacific guyots: Nature, v. 392, p. 889–894, https://doi.org/10.1038/31865.

Worthington, T.J., Hekinian, R., Stoffers, P., Kuhn, T., and Hauff, F., 2006, Osbourn Trough: Structure, geochemistry and implications of a mid-Cretaceous paleospreading ridge in the South Pacific: Earth and Planetary Science Letters, v. 245, p. 685–701, https://doi.org/10.1016/j.epsl.2006.03.018.